Merli Gisbert, R.; Lazaro, C.; Monleón Cremades, S.; Domingo Cabo, A. (2015). Geometrical nonlinear formulation of a Molecular Mechanics model applied to the structural analysis of single-walled carbon nanotubes. International Journal of Solids and Structures. 58:157-177. doi:10.1016/j.ijsolstr.2014.12.028.

Geometrical nonlinear formulation of a Molecular Mechanics model applied to the structural analysis of single-walled carbon nanotubes

R. Merli[*,a], C. Lázaro[a], S. Monleón[a], A. Domingo[b]

[a]*Departamento de Mecánica de los Medios Continuos y Teoría de Estructuras. Escuela Técnica Superior de Ingenieros de Caminos, Canales y Puertos. Universitat Politècnica de València. Camino de vera s/n, 46022 Valencia, Spain*
[b]*Departamento de Ingeniería de la Construcción. Escuela Técnica Superior de Ingenieros de Caminos, Canales y Puertos. Universitat Politècnica de València. Camino de vera s/n, 46022 Valencia, Spain*

Abstract

In this paper, the post-critical behavior and buckling modes of single-walled carbon nanotubes are analyzed via a Molecular Mechanics model. The main target is to develop a general formulation for the model, which has been simplified under small strains assumption, and to implement a versatile tool for the structural analysis of carbon nanotubes in the framework of geometrical nonlinearity. For this purpose, a mechanical formulation able to reproduce any load configuration and supporting conditions has been derived by using an energy approach. Then, an incremental-iterative solution procedure has been implemented in order to trace several nonlinear equilibrium paths and to obtain the corresponding critical strains of clamped-clamped nanotubes under compressive, flexural and torsional loading distributions. The model shows a good numerical performance and results in agreement with previous atomistic works.

Two interatomic potentials have been adopted in order to find out the influence of different constitutive relationships on the final nonlinear response. We have concluded that the choice of the potential function has no significant effect on the final buckling strains. Our results confirm that the final buckling response is strongly determined by geometrical imperfections in the nanotube, which can be well reproduced in the proposed model, but are much more difficult to handle in continuum models.

Key words: Carbon nanotubes, Molecular mechanics, Honeycomb structures, Energy methods, Nonlinear, Buckling strain

1. Introduction

Carbon nanotubes[1] (CNTs) have represented a remarkable centre of attention into the scientific and research community over the past two decades, due to their outstanding mechanical and electrical properties (Dresselhaus et al., 2001). For instance, CNTs show a singular coupling between mechanical strain and electrical conductivity (Paulson et al., 1999; Rochefort et al., 1999), becoming ideal candidates for making nano-sensors (Kang et al., 2006) and nano electro-mechanical systems, with promising applications in robotics and biomechanics. Hence, Liu et al. (2003) studied the flexural buckling of Multi-walled Carbon Nanotubes (MWCNTs) under an electrostatic field and Naieni et al. (2011) dealt with the influence of the transversal deformation of a CNTs cross on the electrical transport. Also, in Rasekh et al. (2010) the nonlinear analysis of clamped-clamped electrostatically actuated CNTs is carried out.

[*]Corresponding author at: Universitat Politècnica de València, Departamento de Mecánica de los Medios Continuos y Teoría de Estructuras. Camino de vera s/n, 46022 Valencia, Spain. Tel:+34 96 387 76 77. Fax: +34 96 387 96 79

Email address: ramergis@doctor.upv.es (R. Merli)

[1]Summary of abbreviations: Carbon nanotube (CNT), Single-walled carbon nanotube (SWCNT), Multi-walled carbon nanotube (MWCNT), Molecular Structural Mechanics (MSM), Molecular Mechanics (MM), Molecular Dynamics (MD), Finite element (FE), Virtual work equation (VWE), Assisted model building with energy refinement (AMBER)

Moreover, CNTs are the stiffest (Young's modulus $\simeq$ 1 TPa, see Hernandez et al. (1998)) and strongest materials ($\sigma_y \simeq 50$ GPa, see Belytschko et al. (2002)) to date. Therefore, carbon nanotube based composites have shown a wide range of potential applications, especially where a high ratio strength-to-weight is needed (e.g. in the aircraft industry). In this field, Ajayan et al. (2000) stated that the strength of the composite is mainly influenced by the low strength of the Single-Walled Carbon Nanotube (SWCNT) bundles but not by the toughness of the isolated SWCNT. However, a deep understanding of the mechanical behavior of SWCNTs is a first step necessary to establish the response of SWCNT bundles. Of course, we should worry about a strong nanotube-matrix interface which could be achieved by chemical functionalization of the CNT ends (Dresselhaus et al., 2001). Moreover, Parnes and Chiskis (2002) examined the buckling of nano-fibres into a polymer matrix and stressed that the buckling failure of nano-fibres could be the prevailing mode of collapse even in reinforced composites.

Taking all the aforementioned issues into account, in this paper we try to gain an insight into the geometrically nonlinear structural behavior of SWCNTs. Our work could be regarded as an initial approach towards the nonlinear behavior of SWCNT bundles involved into a polymer matrix.

To date, many works have been developed to analyze the geometrically nonlinear or buckling response of CNTs and they may be classified into two different categories: atomistic scale and continuum scale methods. The atomistic methods (Molecular Dynamics, ab initio, tight-binding) can successfully reproduce physical phenomena as buckling of MWCNTs (Li et al., 2007; Zhang et al., 2007) or SWCNTs (e.g. Srivastava et al., 1999; Yakobson et al., 1996) under compression, bending or torsion. Nevertheless, these methods have the disadvantage of being limited at a relatively low number of atoms (about 10^9 according to X. Wang et al. (2005)) because of their high computational cost. On the other hand, continuum methods (Arroyo and Belytschko, 2003; Pantano et al., 2004; Wang and Varadan, 2005) are computationally cheaper and capable of analyze longer systems, but the choice of some parameters (as the wall thickness, ranging from $t = 0.066$ nm in Yakobson et al. (1996) to 0.34 nm in Meo and Rossi (2006)) for establishing an equivalence with the atomistic level may be controversial. Furthermore, continuum methods are not able to reproduce either the atomistic structure or the atomistic-scale defects which can modify a great deal the final response of CNTs.

As an intermediate point between atomistic and continuum methods, Molecular Structural Mechanics (MSM) models constitute an alternative tool of analysis which reproduce the atomistic structure in detail but are efficient enough in terms of numerical performance. Some authors (Li and Chou, 2003a; Zaeri et al., 2010) considered SWCNTs as a frame system with carbon atoms located at the nodes and rigid bars representing the covalent bonds. Where MWCNTs were studied (Li and Chou, 2003b; Zaeri et al., 2010), the different layers were connected by several truss rods between neighboring atoms. Alternatively, Odegard et al. (2002) modeled the graphene sheet as a 2D truss model with additional rods through the hexagonal unit cell. However, these kind of models are physically unrealistic because auxiliar elements or stiffnesses were needed in order to introduce the three-body interaction.

Aimed to describe mechanically the SWCNTs more faithfully, the 'stick-spiral' model (Chang and Gao, 2003) reproduces covalent bonds by axial springs and introduces the three-body interaction directly by three spiral springs around each node. Later (see Natsuki et al. (2004); Natsuki and Endo (2004); Xiao et al. (2005)), the same model was adopted to establish some mechanical parameters of SWCNTs and also in Chang et al. (2006) the model was extended to Chiral nanotubes. All the aforementioned references related to MSM limited their calculations to a small unit cell involving only a few atoms subjected to a specific loading distribution. Therefore, a new specific set of equations should be derived for each loading configuration. Otherwise, Meo and Rossi (2006) implemented the 'stick-spiral' model in the finite element (FE) commercial code ANSYS® testing a SWCNT as a whole under each load case, but no formulation of the model was shown. In addition, the implicit loss of accuracy associated to the FE modelling was inherent in their results.

Consequently, our work deals with the 'stick-spiral' model but reformulated in such a way that the equations have general validity regardless of the external loading configuration. Moreover, the equations included herein may be regarded as the geometrically nonlinear extension of our previous work (Merli et al., 2012) in which a review of some mechanical parameters of SWCNTs by means of the same MSM model was provided. In addition, our numerical treatment is rather in the Molecular Mechanics (MM) approach of Cao and Chen (2006).

We would like to highlight the main advantages of the present formulation against the Molecular Dynamics (MD) methods. Despite of the high accuracy yielded by the latter, a system of N particles is described dynamically by a vector of instantaneous positions and velocities (dimension $6N$) but in the former only $3N$ fundamental variables are involved (nodal displacements), which implies a much higher numerical performance of the method. This feature is

specially important in geometrical nonlinear analysis, where the computation of the tangent stiffness matrix and the resolution of the linear incremental system represent a tough task. Also, MSM models are basically static and no time-integration is needed. Finally, in our formulation no heat conduction with the surrounding media is taken into account. However, the real buckling response of isolated SWCNTs is highly influenced by random thermal fluctuation, which constitutes a limitation for MM models. Despite of this fact, the coupling between thermal vibration and structural defects makes difficult to analyze the intrinsic buckling of a SWCNT via MD methods. In this sense, MM or MSM are interesting tools as a first step to understand the basic buckling behavior.

The main contributions of this paper can be outlined as follows:

1. In this paper, the main objective is to find out the geometrical nonlinear behavior of SWCNTs by means of a new general (nonlinear) formulation of the 'stick-spiral' model, in contrast with purely atomistic methods. Therefore, compressive, flexural and torsional simulations were carried out aimed to the plot of nonlinear equilibrium paths and the obtention of critical strains and stresses. For this purpose, analytical expressions have been derived through an energy approach which can reproduce any load conditions with no need of additional equations. Even in geometrical nonlinear analysis with MSM models, some authors (Chang et al., 2005) formulate their equations over a small number of atoms and the corresponding bonds under specific load configurations.
2. An approximate geometrical nonlinear formulation of a generic three-dimensional rotational spring is provided in terms of the nodal displacements involved (see eq. (31)). In spite of the nonlinear formulation of a two-dimensional torsional spring is tackled in some references (see Felippa (2001), as an example), the 3D nonlinear formulation of this kind of springs represents a novelty, up to our knowledge.
3. It is very simple to introduce any interatomic potential function into our formulation provided that the bond lengthening and angular distortion between bonds appear uncoupled. This is not the case in the most frequently used potentials in MD simulations, as the Tersoff-Brenner potential (Brenner, 1990; Tersoff, 1986), but it could be readily approached by the Morse potential (uncoupled) for longitudinal strains below 10% (Belytschko et al., 2002). Aimed to highlight this versatility and further compare results, two interatomic potentials (see section 4) have been implemented in this work.
4. Several nonlinear equilibrium paths and critical strains under each load case are provided as output results of our implemented codes. Also, some deformed shapes for the last iteration into the nonlinear path are included. This results are readily compared with those reported in some published references from MD (or continuum) simulations in order to validate our model.

The paper is organized as follows: in section 2 a schematic description of our model is provided. In section 3 the nonlinear formulation of the MSM model is tackled. In section 4 a brief discussion about the adopted potentials is drawn. Details of the numerical procedures implemented are given in section 5. Numerical results and comparisons with some released references are carried out in section 6 and finally, some concluding remarks are addressed in section 7.

2. Qualitative description of the model

In this section, a brief description of the 'stick-spiral' model is provided. As an example, its geometry and main elements for a ZigZag SWCNT are depicted in figure 1. Covalent $C-C$ bonds are represented by 'truss' (or linear spring) elements which are just axially deformable and the three-body interaction is represented by rotational springs which are exclusively rotational-stiff against angular distortion between two neighboring covalent bonds on each atom. The main degrees of freedom (DOFs) of the model are the linear displacements at each node, therefore angular distortions will be written as functions of them. Accordingly, solely point loads (no moments) will be applied at each node if necessary, and all the boundary conditions are applied by means of pinned joints at the edge nodes of the SWCNTs. In the present work, the load is applied through a set of prescribed displacements at the moving nodes on the atoms of the right end of the SWCNTs, but keeping their circular cross-section arrangement. On the other hand, the atoms of the left end are regarded fixed by pinned joints with zero displacements.

A clamped-clamped scheme has been adopted for our purposes. However, our model is able to meet any kind of load and supporting conditions different from the compressive, flexural or torsional adopted in this paper. Therefore,

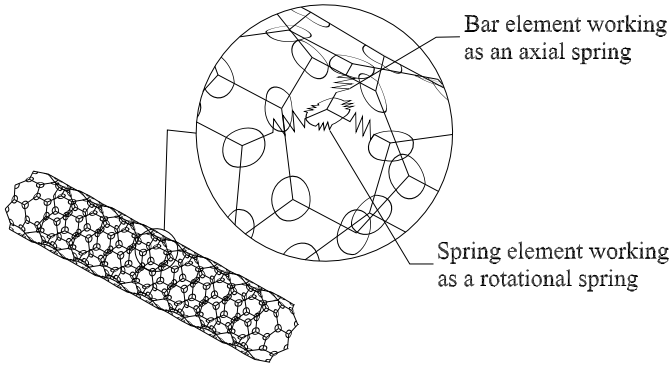

Figure 1: Geometrical description of elements

there is no need to derive particular equations for each loading distribution, in contrast with Chang and Gao (2003); Chang et al. (2006); Xiao et al. (2005).

3. Nonlinear formulation of the MSM model

3.1. Bar element

The following approach may be regarded as the geometrical nonlinear extension of the equations developed in our previous work (Merli et al., 2012) by using the same energy approach. The small displacements assumption has been removed in this case and the necessary nonlinear terms have been included.

Note that our model is not into FE framework, in contrast with Meo and Rossi (2006). In fact, no kinematical interpolation (with the consequent loss of accuracy) is included into the kinematical equations and no shape functions are needed. By contrast, the present model is a MM-based structural model involving direct relationships between each structural member and the interatomic potential.

3.1.1. Kinematic equations

We can define the nonlinear change in length of the bar element representing a covalent C-C bond as:

$$e = \frac{l'^2 - l^2}{2l} \tag{1}$$

Where l, l' stand for the initial and final length of the element [2].

Definition (1) is inspired by the Green's nonlinear axial strain adopted in structural mechanics (see Malvern (1969) as an example), but in our case it has length dimension. In this way, it allows us to write the axial strain virtual energy of the element as $N\delta e$ in a straightforward manner, which will be useful in the further development of the equilibrium equation (7). In addition, the interatomic functions adopted in this work (see section 4) are defined in terms of the change in length of the covalent bond, not in terms of the corresponding axial strain.

We establish now the relations between position vectors and displacements:

$$\mathbf{x}'_i = \mathbf{x}_i + \mathbf{u}^a_i \tag{2a}$$

$$\mathbf{x}'_j = \mathbf{x}_j + \mathbf{u}^a_j \tag{2b}$$

$$\text{and also:} \quad \mathbf{x}_{ij} = \mathbf{x}_j - \mathbf{x}_i = l^a \boldsymbol{\lambda}^a \tag{2c}$$

$$\mathbf{x}'_{ij} = \mathbf{x}'_j - \mathbf{x}'_i = l'^a \boldsymbol{\lambda}'^a \tag{2d}$$

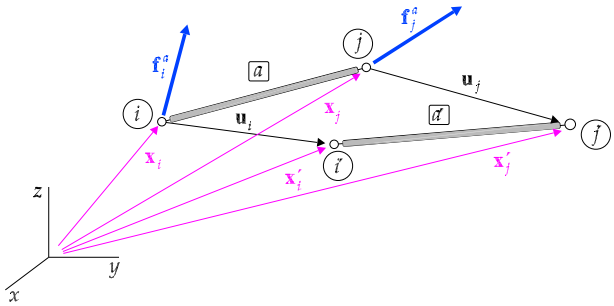

Figure 2: Forces and displacements at the bar ends (color on the Web)

where $\boldsymbol{\lambda}^a$, $\boldsymbol{\lambda}'^a$ denote the unit vectors along the bar element in the initial and deformed configuration respectively and the rest of variables implied in eqs. (2) are described in figure 2.

By subtracting (2a) from (2b) and employing (2c), (2d) we achieve:

$$\boldsymbol{\lambda}'^a = \frac{l^a}{l'^a}\boldsymbol{\lambda}^a + \frac{\mathbf{u}_{ij}^a}{l'^a} \tag{3}$$

At this point, the numerator of definition (1) for the bar element a can be evaluated as [3]:

$$(l'^a)^2 - (l^a)^2 = \mathbf{x}_{ij}'^T\mathbf{x}_{ij}' - \mathbf{x}_{ij}^T\mathbf{x}_{ij} = 2(\mathbf{x}_{ij})^T\mathbf{u}_{ij}^a + (\mathbf{u}_{ij}^a)^T\mathbf{u}_{ij}^a \tag{4}$$

So, next expression for the nonlinear axial strain is rendered:

$$e^a = (\boldsymbol{\lambda}^a)^T\mathbf{u}_{ij}^a + \frac{1}{2l^a}(\mathbf{u}_{ij}^a)^T\mathbf{u}_{ij}^a \tag{5}$$

It should be noted that eq. (5) is the exact expression for the change in length of the bar element with no simplification or *linearization*, just involving quadratic terms in the displacements.

Grouping by blocks into eq (5), we can express the axial strain in terms of a nonlinear kinematic matrix and the nodal displacements as follows:

$$\begin{aligned} e^a = \begin{bmatrix} -(\boldsymbol{\lambda}^a)^T & (\boldsymbol{\lambda}^a)^T \end{bmatrix} \begin{Bmatrix} \mathbf{u}_i^a \\ \mathbf{u}_j^a \end{Bmatrix} + \frac{1}{2}\begin{bmatrix} \mathbf{u}_i^a & \mathbf{u}_j^a \end{bmatrix} \begin{bmatrix} \mathbf{I}/l^a & -\mathbf{I}/l^a \\ -\mathbf{I}/l^a & \mathbf{I}/l^a \end{bmatrix} \begin{Bmatrix} \mathbf{u}_i^a \\ \mathbf{u}_j^a \end{Bmatrix} = \\ = \mathbf{C}_l^a\mathbf{u}^a + \frac{1}{2}(\mathbf{u}^a)^T\mathbf{Z}^a\mathbf{u}^a = \left[\mathbf{C}_l^a + \frac{1}{2}\mathbf{C}_n^a(\mathbf{u}^a)\right]\mathbf{u}^a = \mathbf{C}^a(\mathbf{u}^a)\mathbf{u}^a \end{aligned} \tag{6}$$

where:

$\mathbf{u}^a =$	nodal displacements of the bar element.
$\mathbf{I} =$	identity matrix of size 3×3.
$l^a =$	initial length of the bar element.
$\mathbf{Z}^a =$	auxiliary (constant and symmetric) matrix.
$\mathbf{C}_l^a =$	linear kinematic matrix of the bar element.
$\mathbf{C}_n^a(\mathbf{u}^a) =$	nonlinear kinematic matrix of the bar element.
$\mathbf{C}^a(\mathbf{u}^a) =$	total kinematic matrix of the bar element.

[2] Hereinafter, we will denote by ( )' the variables measured in the deformed configuration of the element

[3] Superscripts $(\,)^a$ have been kept over the nodal displacements by coherence with other variables involved in eqs (2)-(6)

3.1.2. Equilibrium equation

The equilibrium of the bar element at any point of the nonlinear path can be established through the Virtual Work Equation (VWE) for a set of kinematically admissible Lagrangian variations of the end displacements $\delta\mathbf{u}_i^a, \delta\mathbf{u}_j^a$ as:

$$(\mathbf{f}_i^a)^T \delta\mathbf{u}_i^a + (\mathbf{f}_j^a)^T \delta\mathbf{u}_j^a = N^a \delta e^a \tag{7}$$

where $\mathbf{f}_i^a, \mathbf{f}_j^a$ are the end forces of the bar referred to the undeformed configuration (see figure 2) and N^a is the axial force of the bar element pulled-back to the reference configuration.

Moreover, we can evaluate the first variation δe^a by using equation (6) as:

$$\begin{aligned} \delta e^a = \frac{\partial e^a}{\partial \mathbf{u}^a}\delta\mathbf{u}^a &= \left[\mathbf{C}_l^a + \frac{1}{2}(\mathbf{u}^a)^T\mathbf{Z}^a + \frac{1}{2}(\mathbf{Z}^a\mathbf{u}^a)^T\right]\delta\mathbf{u}^a = \\ &= \left[\mathbf{C}_l^a + (\mathbf{u}^a)^T\mathbf{Z}^a\right]\delta\mathbf{u}^a = \left[\mathbf{C}_l^a + \mathbf{C}_n^a(\mathbf{u}^a)\right]\delta\mathbf{u}^a = \mathbf{b}^a(\mathbf{u}^a)\,\delta\mathbf{u}^a \end{aligned} \tag{8}$$

Therefore, substituting into (7) and grouping by blocks:

$$\begin{bmatrix}(\mathbf{f}_i^a)^T & (\mathbf{f}_j^a)^T\end{bmatrix}\begin{Bmatrix}\delta\mathbf{u}_i^a \\ \delta\mathbf{u}_j^a\end{Bmatrix} = N^a\mathbf{b}^a(\mathbf{u}^a)\,\delta\mathbf{u}^a \tag{9a}$$

$$(\mathbf{f}^a)^T\delta\mathbf{u}^a - N^a\mathbf{b}^a(\mathbf{u}^a)\,\delta\mathbf{u}^a = \mathbf{0} \tag{9b}$$

$$\mathbf{f}^a = N^a(\mathbf{b}^a(\mathbf{u}^a))^T = N^a\left[(\mathbf{C}_l^a)^T + (\mathbf{C}_n^a(\mathbf{u}^a))^T\right] \tag{9c}$$

3.1.3. Constitutive equation

In general, a completely uncoupled interatomic potential function U is assumed (more details will be given in section 4), where the contribution of each element is exclusively dependent on its corresponding strain. Therefore, the following constitutive equation for the bar element is stated:

$$N^a = \frac{\partial U}{\partial e^a} = f(e^a) \tag{10}$$

where $f(e^a)$ is a nonlinear function. We are concerned by the incremental constitutive equations from a particular equilibrium point, namely:

$$\begin{aligned} \frac{dN^a}{de^a} &= f'(e^a) = K^a(e^a) \\ dN^a &= K^a(e^a)\,de^a \end{aligned} \tag{11}$$

where K^a is the tangent constitutive stiffness of the bar element. Furthermore, eq. (11) can be written in terms of the coherent Lagrangian variations as:

$$\delta N^a = K^a(e^a)\,\delta e^a \tag{12}$$

3.1.4. Tangent stiffness matrix

The total potential energy F of an elastic system is defined as the difference between the internal and the external work, $F = W_{int} - W_{ext}$. Following Lanczos (1986), if two (infinitely close) equilibrium configurations are considered, the indifferent equilibrium condition may be expressed as:

$$\begin{aligned} \delta^2 F &= 0 \\ \delta^2 W_{int} &= \delta^2 W_{ext} \end{aligned} \tag{13}$$

Therefore, work of internal forces can be written as a quadratic form of the displacements, the kernel of which is the tangent stiffness matrix:

$$\delta^2 W_{int} = \delta\mathbf{u}^T\mathbf{K}_T\delta\mathbf{u} \tag{14}$$

Applying definition (14) to the bar element and using (12) we achieve:

$$\delta^2 W_{int} = \delta(\delta W_{int}) = \delta(N^a \delta e^a) = \delta N^a \delta e^a + N^a \delta^2 e^a = K^a (\delta e^a)^2 + N^a \delta^2 e^a \tag{15}$$

Substituting (8) and taking into account that second variations of displacements $\delta^2 \mathbf{u}^a$ vanish, matrix $\mathbf{K}_T^a$ is readily obtained:

$$\begin{aligned} \delta^2 W_{int} &= \delta(\mathbf{u}^a)^T \left[K^a (\mathbf{b}^a)^T \mathbf{b}^a + N^a \mathbf{Z}^a \right] \delta \mathbf{u}^a \\ \mathbf{K}_T^a &= K^a (\mathbf{b}^a)^T \mathbf{b}^a + N^a \mathbf{Z}^a \end{aligned} \tag{16}$$

3.2. Rotational spring element

3.2.1. Kinematic equations

The interaction between two covalent bonds (so-called *three-body* interaction) is represented in our model by in-plane rotational springs around the differential environment of the central atom, as can be seen in figure 3. Bar elements are not involved in this interaction, but their directions are represented by auxiliary straight lines for the sake of clarity.

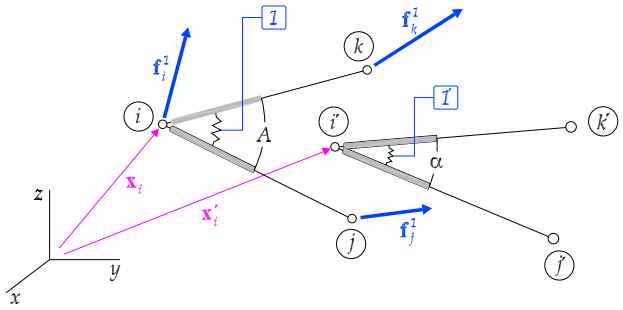

Figure 3: Forces and displacements acting on the spring element (color on the Web)

The nonlinear angular strain in the spring element is defined as the difference in angle between two adjacent covalent bonds from the initial to the deformed shape:

$$e^1 = \Delta\gamma^{ab} = A - \alpha \tag{17}$$

Assuming that strains are small enough, we can *linearize* the equation (17) as follows:

$$\begin{aligned} \alpha &= A - e^1 \\ \cos\alpha &= \cos A \cos e^1 + \sin A \sin e^1 \simeq \cos A + e^1 \sin A \\ e^1 &= \frac{\cos\alpha - \cos A}{\sin A} = \frac{[(\boldsymbol{\lambda}^{a'})^T \boldsymbol{\lambda}^{b'}] - [(\boldsymbol{\lambda}^a)^T \boldsymbol{\lambda}^b]}{\sin A} \end{aligned} \tag{18}$$

The small strains assumption has been accepted even with *moderate* displacements (not arbitrarily large), since the geometrical nonlinearity is previous to the *constitutive* nonlinearity, as has been experimentally reported by Falvo et al. (1997) and theoretically predicted through MD techniques (Iijima et al., 1996; Srivastava et al., 1999; Y. Wang et al., 2005).

We first evaluate $\cos\alpha$ in (18) utilizing (3), so:

$$\cos\alpha = \frac{l^a l^b}{l'^a l'^b} \left[\boldsymbol{\lambda}^a + \frac{\mathbf{u}_{ij}^a}{l^a} \right]^T \left[\boldsymbol{\lambda}^b + \frac{\mathbf{u}_{ik}^b}{l^b} \right] = \frac{1}{\rho_l(\mathbf{u}^a, \mathbf{u}^b)} \left[(\boldsymbol{\lambda}^a)^T \boldsymbol{\lambda}^b + (\boldsymbol{\lambda}^a)^T \frac{\mathbf{u}_{ik}^b}{l^b} + \frac{(\mathbf{u}_{ij}^a)^T}{l^a} \boldsymbol{\lambda}^b + \frac{(\mathbf{u}_{ij}^a)^T \mathbf{u}_{ik}^b}{l^a l^b} \right] \tag{19}$$

where we have defined $\rho_l(\mathbf{u}^a, \mathbf{u}^b)$ as a function of the nodal displacements which can be developed as:

$$\rho_l(\mathbf{u}^a, \mathbf{u}^b) = \frac{l'^a l'^b}{l^a l^b} = \frac{(l^a + e^a)(l^b + e^b)}{l^a l^b} = 1 + \frac{e^a}{l^a} + \frac{e^b}{l^b} + \frac{e^a e^b}{l^a l^b} = 1 + \eta(\mathbf{u}^a, \mathbf{u}^b) \tag{20}$$

Next, eq.(5) is substituted into the auxiliary function $\eta(\mathbf{u}^a, \mathbf{u}^b)$ to produce:

$$\eta(\mathbf{u}^a, \mathbf{u}^b) = \frac{(\boldsymbol{\lambda}^a)^T}{l^a}\mathbf{u}^a_{ij} + \frac{1}{2l^{a2}}(\mathbf{u}^a_{ij})^T\mathbf{u}^a_{ij} + \frac{(\boldsymbol{\lambda}^b)^T}{l^b}\mathbf{u}^b_{ik} + \frac{1}{2l^{b2}}(\mathbf{u}^b_{ik})^T\mathbf{u}^b_{ik} +$$
$$+ \frac{1}{l^a l^b}\left\{\left((\boldsymbol{\lambda}^a)^T\mathbf{u}^a_{ij}\right)\left((\boldsymbol{\lambda}^b)^T\mathbf{u}^b_{ik}\right) + \frac{1}{2l^b}\left((\boldsymbol{\lambda}^a)^T\mathbf{u}^a_{ij}\right)\left((\mathbf{u}^b_{ik})^T\mathbf{u}^b_{ik}\right) + \frac{1}{2l^a}\left((\mathbf{u}^a_{ij})^T\mathbf{u}^a_{ij}\right)\left((\boldsymbol{\lambda}^b)^T\mathbf{u}^b_{ik}\right) + \frac{1}{4l^a l^b}\left((\mathbf{u}^a_{ij})^T\mathbf{u}^a_{ij}\right)\left((\mathbf{u}^b_{ik})^T\mathbf{u}^b_{ik}\right)\right\} \tag{21}$$

According with the expression (5) for the nonlinear change in length, the nonlinear angular strain is assumed to be small enough in such a way that third and successive terms of displacements can be neglected in the following equations. More precisely, we can write:

$$\mathbf{u}_{\alpha\beta} = \varepsilon\overline{\mathbf{u}}_{\alpha\beta} \qquad\qquad \alpha\beta = ij,\ ik,\ jk \tag{22}$$

where $\overline{\mathbf{u}}_{\alpha\beta}$ are a set of relative displacements kinematically admissible of bounded norm and ε is a scalar value which provide its order of magnitude. Thus:

$$\|\mathbf{u}_{\alpha\beta}\| \leq \varepsilon \qquad\qquad \alpha\beta = ij,\ ik,\ jk \tag{23}$$

and, of course:

$$\varepsilon^3 \ll \varepsilon^2 \qquad\qquad \varepsilon^4 \ll \varepsilon^3 \tag{24}$$

Applying conditions (23) to eq. (21), the following expression may be stated:

$$\|\eta(\mathbf{u}^a, \mathbf{u}^b)\| \simeq \frac{\varepsilon}{l^a} + \frac{\varepsilon}{l^b} + \frac{\varepsilon^2}{2l^{a2}} + \frac{\varepsilon^2}{2l^{b2}} + \frac{\varepsilon^2}{l^a l^b} + O(\varepsilon^n) \qquad\qquad n \geq 3 \tag{25}$$

and taking (24) into account, $\eta(\mathbf{u}^a, \mathbf{u}^b)$ may be simplified as:

$$\eta(\mathbf{u}^a, \mathbf{u}^b) \simeq \frac{(\boldsymbol{\lambda}^a)^T}{l^a}\mathbf{u}^a_{ij} + \frac{1}{2l^{a2}}(\mathbf{u}^a_{ij})^T\mathbf{u}^a_{ij} + \frac{(\boldsymbol{\lambda}^b)^T}{l^b}\mathbf{u}^b_{ik} + \frac{1}{2l^{b2}}(\mathbf{u}^b_{ik})^T\mathbf{u}^b_{ik} + \frac{1}{l^a l^b}(\mathbf{u}^a_{ij})^T\left[\boldsymbol{\lambda}^a(\boldsymbol{\lambda}^b)^T\right]\mathbf{u}^b_{ik} \tag{26}$$

Adopting (26) in eqs. (19) and (20), and substituting into definition (18):

$$e^1 = \frac{1}{(1 + \eta(\mathbf{u}^a, \mathbf{u}^b))\sin A}\left\{(\boldsymbol{\lambda}^a)^T\frac{\mathbf{u}_{ik}}{l^b} + (\boldsymbol{\lambda}^b)^T\frac{\mathbf{u}_{ij}}{l^a} + \frac{(\mathbf{u}_{ik})^T\mathbf{u}_{ik}}{l^a l^b} - \eta(\mathbf{u}^a, \mathbf{u}^b)\cos A\right\} \tag{27}$$

Derived from conditions (24), it is obvious to establish $\|\eta(\mathbf{u}^a, \mathbf{u}^b)\| \simeq O(\varepsilon) \ll 1$. Therefore, function η can be neglected in the denominator of (27) and operating:

$$e^1 = \left[\frac{(\boldsymbol{\lambda}^b)^T}{l^a\sin A} - \frac{(\boldsymbol{\lambda}^a)^T}{l^a\tan A}\right]\mathbf{u}^a_{ij} + \left[\frac{(\boldsymbol{\lambda}^a)^T}{l^b\sin A} - \frac{(\boldsymbol{\lambda}^b)^T}{l^b\tan A}\right]\mathbf{u}^b_{ik} + \frac{(\mathbf{u}^a_{ij})^T\mathbf{u}^b_{ik}}{l^a l^b\sin A} - \frac{(\mathbf{u}^a_{ij})^T\mathbf{u}^a_{ij}}{2l^{a2}\tan A} - \frac{(\mathbf{u}^b_{ik})^T\mathbf{u}^b_{ik}}{2l^{b2}\tan A} - \frac{(\mathbf{u}^b_{ij})^T\left[\boldsymbol{\lambda}^a(\boldsymbol{\lambda}^b)^T\right]\mathbf{u}^b_{ik}}{l^a l^b\tan A} \tag{28}$$

For simplicity, the following definitions are adopted:

$$\boldsymbol{\Gamma}^1_j = \left[\frac{\boldsymbol{\lambda}^b}{l^a\sin A} - \frac{\boldsymbol{\lambda}^a}{l^a\tan A}\right] \qquad \boldsymbol{\Gamma}^1_k = \left[\frac{\boldsymbol{\lambda}^a}{l^b\sin A} - \frac{\boldsymbol{\lambda}^b}{l^b\tan A}\right] \qquad \boldsymbol{\Gamma}^1_i = -\boldsymbol{\Gamma}^1_j - \boldsymbol{\Gamma}^1_k \tag{29a}$$

$$\omega_a = \frac{1}{l^{a2}\tan A} \qquad \omega_b = \frac{1}{l^{b2}\tan A} \qquad \omega_{ab} = \frac{1}{l^a l^b\sin A} \tag{29b}$$

$$\boldsymbol{\Lambda}_{ab} = \mathbf{I} - \boldsymbol{\lambda}^a(\boldsymbol{\lambda}^b)^T\cos A \tag{29c}$$

In this way, (28) becomes:

$$e^1 = {\boldsymbol{\Gamma}_j^1}^T \mathbf{u}_{ij}^a + {\boldsymbol{\Gamma}_k^1}^T \mathbf{u}_{ik}^b + \omega_{ab} (\mathbf{u}_{ij}^a)^T \boldsymbol{\Lambda}_{ab} \mathbf{u}_{ik}^b - \frac{\omega_a}{2} (\mathbf{u}_{ij}^a)^T \mathbf{u}_{ij}^a - \frac{\omega_b}{2} (\mathbf{u}_{ik}^b)^T \mathbf{u}_{ik}^b \tag{30}$$

Rearranging terms and grouping by blocks, (30) can be transformed into:

$$\begin{aligned} e^1 &= \begin{bmatrix} {\boldsymbol{\Gamma}_j^1}^T & {\boldsymbol{\Gamma}_i^1}^T & {\boldsymbol{\Gamma}_k^1}^T \end{bmatrix} \begin{Bmatrix} \mathbf{u}_j^1 \\ \mathbf{u}_i^1 \\ \mathbf{u}_k^1 \end{Bmatrix} + \\ &+ \frac{1}{2} \begin{bmatrix} {\mathbf{u}_j^1}^T & {\mathbf{u}_i^1}^T & {\mathbf{u}_k^1}^T \end{bmatrix} \begin{bmatrix} -\omega_a \mathbf{I} & \omega_a \mathbf{I} - \omega_{ab} \boldsymbol{\Lambda}_{ab} & \omega_{ab} \boldsymbol{\Lambda}_{ab} \\ \omega_a \mathbf{I} - \omega_{ab} \boldsymbol{\Lambda}_{ab}^T & \omega_{ab} (\boldsymbol{\Lambda}_{ab} + \boldsymbol{\Lambda}_{ab}^T) - (\omega_a + \omega_b) \mathbf{I} & \omega_b \mathbf{I} - \omega_{ab} \boldsymbol{\Lambda}_{ab} \\ \omega_{ab} \boldsymbol{\Lambda}_{ab}^T & \omega_b \mathbf{I} - \omega_{ab} \boldsymbol{\Lambda}_{ab}^T & -\omega_b \mathbf{I} \end{bmatrix} \begin{Bmatrix} \mathbf{u}_j^1 \\ \mathbf{u}_i^1 \\ \mathbf{u}_k^1 \end{Bmatrix} = \\ &= \mathbf{C}_l^1 \mathbf{u}^1 + \frac{1}{2} (\mathbf{u}^1)^T \mathbf{Z}^1 \mathbf{u}^1 = \left[\mathbf{C}_l^1 + \frac{1}{2} \mathbf{C}_n^1 (\mathbf{u}^1) \right] \mathbf{u}^1 = \mathbf{C}^1 (\mathbf{u}^1)\, \mathbf{u}^1 \end{aligned} \tag{31}$$

where:

$\mathbf{u}^1 =$ nodal displacements of the rotational spring element.
$\boldsymbol{\Lambda}_{ab} =$ auxiliary (constant and non-symmetric) matrix, dimensions 3×3.
$\mathbf{Z}^1 =$ auxiliary (constant and symmetric) matrix.
$\mathbf{C}_l^1 =$ linear kinematic matrix of the rotational spring element.
$\mathbf{C}_n^1(\mathbf{u}^1) =$ nonlinear kinematic matrix of the rotational spring element.
$\mathbf{C}^1(\mathbf{u}^1) =$ total kinematic matrix of the rotational spring element.

As can be checked, expression (31) has the same structure as (6) in terms of the corresponding nodal displacements, although the matrices involved have different dimensions.

3.2.2. Equilibrium equation

Similarly to eq. (7), the VWE of the rotational spring element at any point of the nonlinear equilibrium path can be written as:

$$(\mathbf{f}_j^1)^T \delta \mathbf{u}_j^1 + (\mathbf{f}_i^1)^T \delta \mathbf{u}_i^1 + (\mathbf{f}_k^1)^T \delta \mathbf{u}_k^1 = M^1 \delta e^1 \tag{32}$$

where $\mathbf{f}_j^1, \mathbf{f}_i^1, \mathbf{f}_k^1$ are the fraction of the external forces contributing to the angular distortion e^1 of the element, referred to the reference configuration. Of course, M^1 is the moment of the rotational spring element pulled-back to the initial state.

As well, δe^1 can be properly evaluated by using eq. (31):

$$\begin{aligned} \delta e^1 = \frac{\partial e^1}{\partial \mathbf{u}^1} \delta \mathbf{u}^1 &= \left[\mathbf{C}_l^1 + \frac{1}{2} (\mathbf{u}^1)^T \mathbf{Z}^1 + \frac{1}{2} (\mathbf{Z}^1 \mathbf{u}^1)^T \right] \delta \mathbf{u}^1 = \\ &= \left[\mathbf{C}_l^1 + (\mathbf{u}^1)^T \mathbf{Z}^1 \right] \delta \mathbf{u}^1 = \left[\mathbf{C}_l^1 + \mathbf{C}_n^1 (\mathbf{u}^1) \right] \delta \mathbf{u}^1 = \mathbf{b}^1 (\mathbf{u}^1)\, \delta \mathbf{u}^1 \end{aligned} \tag{33}$$

Thereupon, substituting into the VWE (32) and grouping by blocks:

$$\begin{bmatrix} (\mathbf{f}_j^1)^T & (\mathbf{f}_i^1)^T & (\mathbf{f}_k^1)^T \end{bmatrix} \begin{Bmatrix} \delta \mathbf{u}_j^1 \\ \delta \mathbf{u}_i^1 \\ \delta \mathbf{u}_k^1 \end{Bmatrix} = M^1 \mathbf{b}^1 (\mathbf{u}^1)\, \delta \mathbf{u}^1 \tag{34a}$$

$$(\mathbf{f}^1)^T \delta \mathbf{u}^1 - M^1 \mathbf{b}^1 (\mathbf{u}^1)\, \delta \mathbf{u}^1 = \mathbf{0} \tag{34b}$$

$$\mathbf{f}^1 = M^1 (\mathbf{b}^1 (\mathbf{u}^1))^T = M^1 \left[(\mathbf{C}_l^1)^T + (\mathbf{C}_n^1 (\mathbf{u}^1))^T \right] \tag{34c}$$

3.2.3. Constitutive equation

Assuming a completely uncoupled potential function U (see section 4), the constitutive equation for the rotational spring element may be stated as:

$$M^1 = \frac{\partial U}{\partial e_1^1} = g(e^1) \tag{35}$$

where $g(e^1)$ is a general nonlinear function of the angular strain e^1. As we did for the bar element, the corresponding incremental and variational constitutive equations have the following form:

$$dM^1 = g'(e^1)de^1 = K^1(e^1)\, de^1 \tag{36a}$$

$$\delta M^1 = K^1(e^1)\, \delta e^1 \tag{36b}$$

where $K^1(e^1)$ is the tangent constitutive stiffness of the rotational spring element.

3.2.4. Tangent stiffness matrix

Definition (14) applied to the rotational spring element is adopted to obtain its tangent stiffness matrix. As well, eq. (36b) is employed in the next expression:

$$\delta^2 W_{int} = \delta(\delta W_{int}) = \delta(M^1 \delta e^1) = \delta M^1 \delta e^1 + M^1 \delta^2 e^1 = K^1(\delta e^1)^2 + M^1 \delta^2 e^1 \tag{37}$$

Substituting (33) and taking into account that second variations of displacements $\delta^2\mathbf{u}^1$ vanish, matrix $\mathbf{K}_T^1$ is readily obtained:

$$\delta^2 W_{int} = \delta(\mathbf{u}^1)^T \left[K^1(\mathbf{b}^1)^T\mathbf{b}^1 + M^1\mathbf{Z}^1\right]\delta\mathbf{u}^1$$

$$\mathbf{K}_T^1 = K^1(\mathbf{b}^1)^T\mathbf{b}^1 + M^1\mathbf{Z}^1 \tag{38}$$

3.3. Whole structural system

This section concerns the geometrical nonlinear analysis of a general set of bars and spring elements properly connected. Namely, those group of elements reproducing SWCNT geometry (fig 1) are treated. Although it has not been explicitly derived in this paper, it is easy to show that the standard boolean assembly of the global stiffness matrix from the individual matrices of each element works properly into this MSM model. In the same way, the kinematical and equilibrium equations can be assembled by arranging adequately blocks of the corresponding individual elements into the global matrices.

For the purpose of defining the incremental stiffness system, the next variables are defined:

$\mathbf{u}_R =$ displacements of free nodes.
$\mathbf{u}_M =$ displacements of moving nodes. Herein $\mathbf{u}_M = \overline{\mathbf{u}}$ are known functions of prescribed displacements.
$\mathbf{f}_R =$ external point loads applied at the free nodes.
$\mathbf{f}_M =$ reactions at the moving nodes.
$\lambda =$ load factor.
$\mathbf{q} =$ vector of incremental load.
$\boldsymbol{\epsilon} =$ vector of incremental imperfection-load.

Grouping by blocks the reduced tangent stiffness matrix, the corresponding incremental stiffness system (from an equilibrium configuration) can be written in the following way:

$$\begin{Bmatrix}\Delta\mathbf{f}_R\\ \Delta\mathbf{f}_M\end{Bmatrix} = \begin{bmatrix}\mathbf{K}_R & \mathbf{K}_{RM}\\ \mathbf{K}_{MR} & \mathbf{K}_M\end{bmatrix}\begin{Bmatrix}\Delta\mathbf{u}_R\\ \Delta\mathbf{u}_M\end{Bmatrix} \tag{39}$$

Developing the first matricial equation of (39) and introducing a known set of prescribed displacements $\Delta\mathbf{u}_M = \Delta\overline{\mathbf{u}}$, we achieve:

$$\Delta\mathbf{f}_R - \mathbf{K}_{RM}\Delta\overline{\mathbf{u}} = \mathbf{K}_R\Delta\mathbf{u}_R \tag{40}$$

Taking into account that external loads and imposed displacements grow proportionally to a load factor λ, eq. (40) may be rewritten as:

$$\Delta\mathbf{f}_R - \mathbf{K}_{RM}\Delta\overline{\mathbf{u}} = \Delta\lambda\boldsymbol{\epsilon} + \Delta\lambda\overline{\mathbf{q}} = \mathbf{K}_R\Delta\mathbf{u}_R$$

$$\Delta\lambda\mathbf{q} = \Delta\lambda(\boldsymbol{\epsilon} + \overline{\mathbf{q}}) = \mathbf{K}\Delta\mathbf{u} \tag{41}$$

where the vector of incremental load $\mathbf{q}$ is formed by a first term $\boldsymbol{\epsilon}$ representing a set of small imperfection-loads at the start of the loading process and a second term $\overline{\mathbf{q}}$ referred to as the vector of incremental load equivalent to the imposed displacements. In normal conditions, the imperfections $\boldsymbol{\epsilon}$ are not present and only the second term is included. For simplicity, the subscripts of the right-hand side in (41) have been omitted.

4. Interatomic potentials

In this section, a brief overwiew of the most usual interatomic potential functions adopted to reproduce the mechanical behavior of SWCNTs is given. This functions can be classified into two main categories:

1. *Harmonic-like potentials*.- In many references related to the 'stick-spiral' model (Chang and Gao, 2003; Lau et al., 2004; Natsuki et al., 2004; Wang, 2004), the harmonic function is limited to the addition of two fundamental terms, namely:

$$U = \sum \frac{1}{2} k_r (\Delta r)^2 + \sum \frac{1}{2} k_\theta (\Delta\theta)^2 \tag{42}$$

where k_r, k_θ are the force constants related to bond lengthening Δr the angular distortion $\Delta\theta$ respectively. The first sum is extended over all covalent bonds and the second over all angles between bonds.
In this paper, constants of the Assisted Model Building with Energy Refinement (AMBER) force field are adopted in eq. (42). Regarding eqs.(10), (11) and (36) and following Li and Chou (2003a); Natsuki et al. (2004); Zaeri et al. (2010), the following tangent constitutive stiffnesses are adopted:

$$K^\alpha = k_r = 652 \text{ nN·nm}^{-1} \qquad \alpha = a, b, c, \ldots \tag{43a}$$

$$K^\beta = k_\theta = 0.876 \text{ nN·nm·rad}^{-1} \qquad \beta = 1, 2, 3, \ldots \tag{43b}$$

Therefore when the AMBER potential has been taken into account, linear constitutive relationships force-strain and moment-distortion have been implemented.

2. *Multi-body potentials*.- The so-called Reactive Empirical Bond Order potentials include the effect of the rest of atoms in the two-body terms of the potential function. Therefore, the effect of bond stretching and angular distortion are coupled into the potential function. The most widely used (e.g. Arroyo and Belytschko, 2003; Iijima et al., 1996; Li et al., 2007; Robertson et al., 1992; Yakobson et al., 1996) potential function (mainly in MD simulations) is the Tersoff-Brenner potential (Brenner, 1990; Tersoff, 1986). However, it can be readily approached by the Morse potential (Belytschko et al., 2002; Natsuki and Endo, 2004) for longitudinal strains below 10%, which is a fully uncoupled function given by:

$$E = \sum E_r + \sum E_\theta \tag{44a}$$

$$E_r = D_e\{[1 - e^{-\beta(\Delta r)}]^2 - 1\} \tag{44b}$$

$$E_\theta = \frac{1}{2} k_\theta (\Delta\theta)^2 [1 + k_s (\Delta\theta)^4] \tag{44c}$$

where the parameters involved take the following values (Belytschko et al., 2002):

$$D_e = 0.2895 \text{ nN·nm} \qquad \beta = 38.43 \text{ nm}^{-1}$$

$$k_\theta = 0.8998 \text{ nN·nm} \qquad k_s = 0.754 \text{ rad}^{-4} \tag{45}$$

Δr is the change in length of covalent bonds from their initial distance of equilibrium in the nanotube, which is around 0.142 nm, and $\Delta\theta$ is the change in angle from the initial one in the SWCNT, which is about $2\pi/3$.
Taking into account eqs.(10), (11) and (36), the tangent constitutive stiffnesses are the second derivatives of the Morse function with respect to the corresponding strain:

$$K^\alpha = 2\beta^2 D_e e^{-\beta(\Delta r^\alpha)} [2e^{-\beta(\Delta r^\alpha)} - 1] \qquad \alpha = a, b, c, \ldots \tag{46a}$$

$$K^\beta = k_\theta [1 + 15 k_s (\Delta\theta^\beta)^4] \qquad \beta = 1, 2, 3, \ldots \tag{46b}$$

Of course, this potential function renders nonlinear constitutive relationships besides the geometrical nonlinearity into the numerical procedure.

Falvo et al. (1997) experimentally reported that MWCNTs are able to experiment bending and buckling up to large displacements, but in the linear range of strains. Hence, the geometrical instability appears before the constitutive nonlinearity. As well, Srivastava et al. (1999), Iijima et al. (1996) and Y. Wang et al. (2005) stated the same conclusion by means of MD calculations. Since one of the main goals of this work is to check numerically this issue for SWCNTs and to find out how much the geometrical nonlinearity is influenced by the constitutive nonlinearity, calculations with both potentials were carried out and their results finally compared.

5. Numerical implementation

In order to find out the critical strains and forces of SWCNTs under several load cases, the tracing of nonlinear equilibrium paths through the so-called *continuation* methods has been numerically implemented. In fact, nonlinear incremental-iterative procedures have been developed, which try to find out a new equilibrium configuration starting from a known equilibrium situation repeatedly.

5.1. Approach of the numerical problem

Following the notation used by Felippa (2001), let us assume that all the variables of the equilibrium state (loads, displacements, strains, forces and so on) grow in proportion to a parameter λ (so-called load factor). Moreover, n incremental steps of the equilibrium analysis have been performed and the last accepted solution is $\mathbf{u}_n, \lambda_n$. At this point, the target is to find out the next equilibrium solution

$$\mathbf{u}_{n+1} = \mathbf{u}_n + \Delta\mathbf{u}_n$$

$$\lambda_{n+1} = \lambda_n + \Delta\lambda_n$$

that satisfies the nonlinear algebraic system:

$$\mathbf{r}(\mathbf{u}_{n+1}, \lambda_{n+1}) = \mathbf{0} \tag{47a}$$

$$c(\Delta\mathbf{u}_n, \Delta\lambda_n) = 0 \tag{47b}$$

where $\mathbf{r}$ is the residual of the nonlinear problem and c is the constraint equation of the control strategy. Hereinafter, subscript n is referred to the current incremental step.

The general form of the nonlinear residual equation is:

$$\mathbf{r}(\mathbf{u}, \lambda) = \mathbf{K}(\mathbf{u})\,\mathbf{u} - \lambda\mathbf{q} \tag{48}$$

On the other hand, an arc-length control strategy has been adopted because it is able to go through the limit points which will appear on the equilibrium path, in contrast with the force control strategy. If a small enough increment step is considered, constraint (47b) takes the form:

$$c(\Delta\mathbf{u}_n, \Delta\lambda_n) = \mathbf{v}_n{}^T \Delta\mathbf{u}_n + \Delta\lambda_n - \Delta s_n f_n = 0 \tag{49}$$

where:

$\Delta s_n = l_0$	constant value adopted for the arc-length over the nonlinear equilibrium path.
$\mathbf{v}_n = \mathbf{K}^{-1}(\mathbf{u}_n)\,\mathbf{q}_n$	incremental velocity vector.
$f_n = \sqrt{1 + \mathbf{v}_n^T \mathbf{v}_n}$	scaling factor.

The conventional Newton-like methods are based on the truncated Taylor expansion (neglecting second and higher order terms) of the system (47) around $\mathbf{u}_n^k, \lambda_n^k$, where superscript k is related to the iteration step. So that, by using eqs. (48) and (49) and introducing $\mathbf{d}_n^k = \Delta\mathbf{u}_n^k$, $\eta_n^k = \Delta\lambda_n^k$ the *augmented stiffness* system is given by:

$$\begin{bmatrix} \mathbf{K}(\mathbf{u}_n^k) & -\mathbf{q}_n^k \\ \mathbf{v}_n^{k\,T} & 1 \end{bmatrix} \begin{Bmatrix} \mathbf{d}_n^k \\ \eta_n^k \end{Bmatrix} = - \begin{Bmatrix} \mathbf{r}_n^k \\ c_n^k \end{Bmatrix} \tag{50}$$

where the variables involved has been defined in 3.3. Note that (50) is the governing system for the *corrective* phase.

5.2. Description of the incremental-iterative procedure

Implementation of the governing equations has been carried out in C++ programming language. As well, the geometry generation of SWCNTs has been developed in VisualLISP code. Aimed to describe graphically the calculation kernel, the general flow diagram has been depicted in figure 4 and more detailed explanations for the predictive and corrective stages into a generic increment have been included in figures 5(a) and 5(b) respectively.

In order to improve the clarity of the figures 4 and 5, several remarks should be noted:

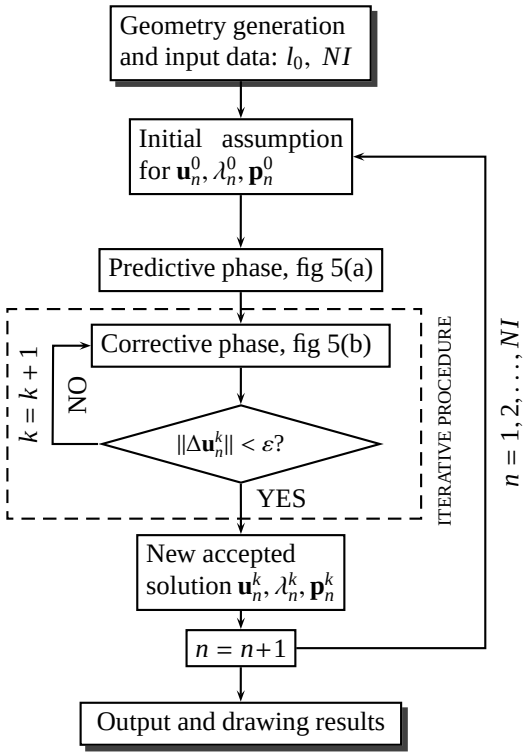

Figure 4: Diagram flow of the incremental-iterative numerical procedure

a. The input data l_0 means the arc-length increment size and NI the number of increments to plot over the nonlinear equilibrium path. These values have been tested out into each simulation in order to reproduce a long branch in the post-critical behavior before the divergence of the numerical process took place (see section 6.4) . As output results, we will get the corresponding equilibrium path and the final forces, reactions and deformed shape in the last increment.
b. Although a convergence condition over the residual could be chosen, the condition indicated in fig 4 regarding the norm of the displacements, taking $\varepsilon = 10^{-6}$, has been preferred for the iterative procedure. Thus, the standard maximum norm criterion has been adopted.
c. The vector $\mathbf{p} = [\mathbf{n} \;\; \mathbf{m}]^T$ contains the internal forces of the whole structural system, where $\mathbf{n}$ are the bar axial forces and $\mathbf{m}$ are the rotational spring moments. Correspondingly, $\mathbf{e} = \left[\mathbf{e}^\alpha \;\; \mathbf{e}^\beta\right]^T$ corresponds to the nonlinear strain vector, where $\mathbf{e}^\alpha$ are the changes in length and $\mathbf{e}^\beta$ are the changes in angle.
d. In general, the initial configuration for the first increment has been assumed as $\mathbf{u}_1^0 = \mathbf{0}, \lambda_1^0 = 0, \mathbf{p}_1^0 = \mathbf{0}$.
e. Regarding the vector of incremental load $\mathbf{q} = \boldsymbol{\epsilon} + \overline{\mathbf{q}}$, the fist term stands for the initial imperfections and are introduced exclusively in the first increment in order to convert the bifurcation points that will appear at the equilibrium path (critical buckling modes) into limit points, which are easier to cross over without divergence of the algorithm. In the following increments, only the second term associated with the prescribed displacements is kept, which can be calculated as (see eq. (41)):

$$\Delta\overline{\mathbf{u}} = \Delta\lambda\widetilde{\mathbf{d}} \tag{51a}$$

$$\Delta\lambda\overline{\mathbf{q}} = -\Delta\lambda\mathbf{K}_{RM}\widetilde{\mathbf{d}} \tag{51b}$$

$$\overline{\mathbf{q}} = -\mathbf{K}_{RM}\widetilde{\mathbf{d}} = -\widetilde{\mathbf{K}}\widetilde{\mathbf{d}} \tag{51c}$$

where $\widetilde{\mathbf{d}}$ are referred to as the incremental prescribed displacements at the moving nodes. Since the first term of the

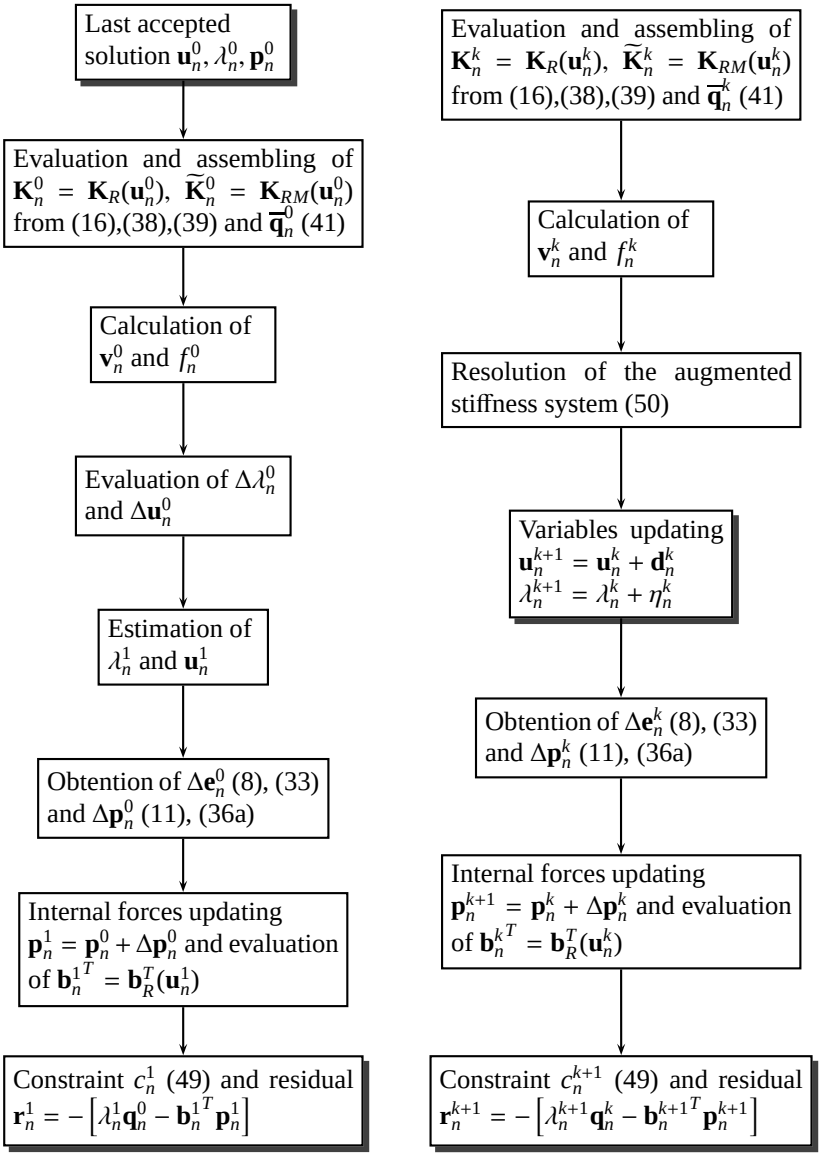

(a) Predictive (incremental) phase (b) Corrective (iterative) phase

Figure 5: Partition of a generic increment

residual just includes the actual external loads and not the *pseudo-loads* $\overline{\mathbf{q}}$, it vanishes from the second increment.

f. The matrix $\mathbf{b}_R(\mathbf{u})$ is constructed from the correct assembling of the $\mathbf{b}$ matrices related to the individual structural elements (see eqs. (8) and (33)) and the corresponding incremental kinematical equation including the prescribed displacements may be written:

$$\Delta\mathbf{e} = \mathbf{b}_R(\mathbf{u})\Delta\mathbf{u} + \mathbf{b}_{RM}(\mathbf{u})\Delta\lambda\widetilde{\mathbf{d}} \tag{52}$$

g. In the incremental constitutive equations, similar to eqs. (11) and (36a), the constitutive tangent stiffnesses given by (43) or (46) are utilized. Namely, a specific code has been developed with AMBER potential and another one with Morse potential in order to check numerically whether the geometrical nonlinearity is previous to the *constitutive*

nonlinearity, as has been theoretically expected (Iijima et al., 1996; Srivastava et al., 1999; Y. Wang et al., 2005), and experimentally reported (Falvo et al., 1997).

h. It may be remarked that the increments $\Delta\mathbf{u}_n, \Delta\lambda_n$ in the constraint (49) should be taken from the start of each incremental step, but no between two consecutive iterations.

6. Numerical results and discussion

In this section, nonlinear geometrical behavior of SWCNTs is studied through compressive, flexural and torsional simulations. Our main objective is to obtain the critical load factor for each loading scheme and to compare the final results with some atomistic simulations.

6.1. Compressive behavior

The nanotubes indicated in table 1 have been chosen under compression.

Chirality	d(nm)	L(nm)	L/d
Armchair(3,3)	0.407	4.919	12.09
Armchair(4,4)	0.542	6.641	12.24
ZigZag(5,0)	0.391	4.757	12.15
ZigZag(7,0)	0.548	6.674	12.18
Chiral(4,2)	0.414	5.072	12.24
Chiral(5,3)	0.548	6.859	12.52

Table 1: Geometrical parameters of SWCNTs under compression

Similar diameters and aspect ratios have been chosen in order to further comparison of the obtained results. Supporting conditions and imposed displacements under compressive loads are displayed in figure 6. Hence, the known function adopted for the prescribed displacements at each pinned joint at the right end of the SWCNT has been:

$$\Delta\overline{\mathbf{u}}_n = \Delta\lambda_n \begin{Bmatrix} -1 \\ 0 \\ 0 \end{Bmatrix} \tag{53}$$

Since the x-axis is oriented parallel to the cylinder axis (fig. 6), $\Delta\lambda_n$ corresponds directly with the incremental shortening of the nanotube. Therefore, equation (53) describes a rigid body translation of the right end cross section towards the left end.

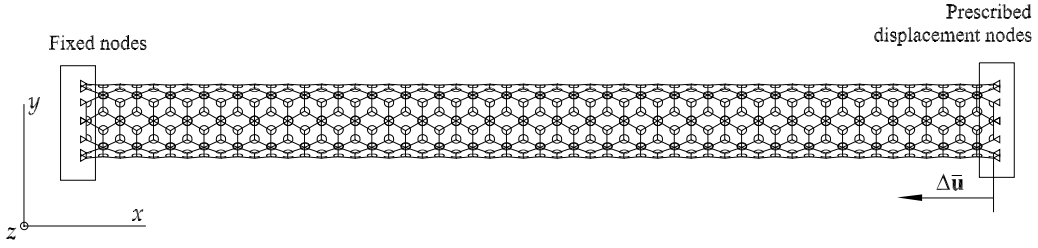

Figure 6: Supporting conditions under compressive loads

As has been mentioned before, two calculations have been performed for each nanotube of table 1 (with one different potential each). Since two-dimensional plots are easier to understand for the nonlinear equilibrium paths, the transversal displacement u_ρ of a representative node around the midpoint of the SWCNT has been represented against the load parameter λ. Some of the equilibrium paths and final deformed shapes as examples of the obtained global buckling behavior are given in figures 7 and 8 respectively.

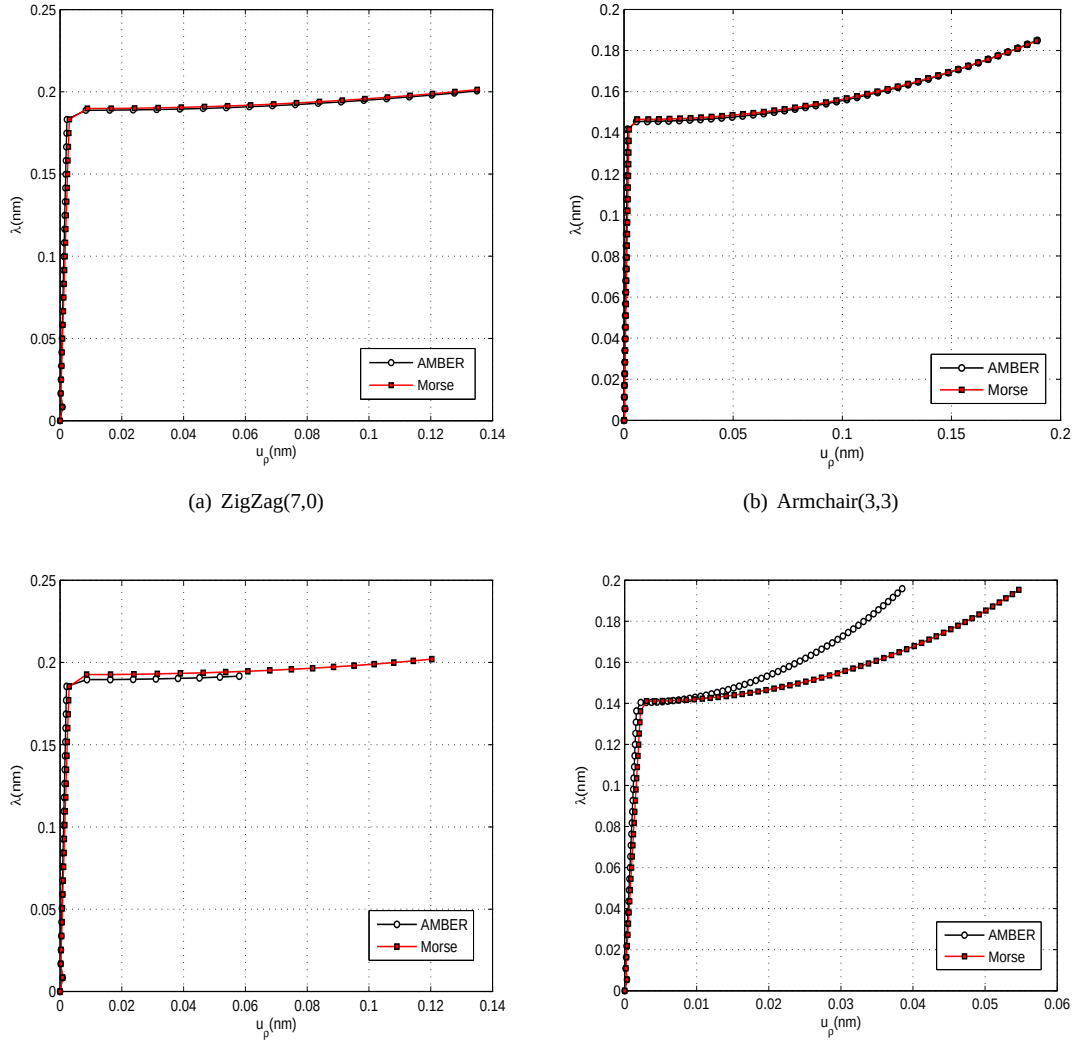

(a) ZigZag(7,0)

(b) Armchair(3,3)

(c) Armchair(4,4)

(d) Chiral(4,2)

Figure 7: Nonlinear equilibrium paths under compression (color on the Web)

Initial imperfections in all simulations under compression have been adopted as a set of point transversal loads on the nodes located at the cross-section around the midpoint of the nanotube, the values of which have been tested out trying to achieve the longest curve after buckling without divergence of the numerical algorithm. In fact, some values of these imperfections produce the divergence of the process before buckling took place (see section 6.4).

For each critical load factor obtained from the equilibrium paths, the equivalent axial strain has been evaluated as:

$$\varepsilon_{cr} = \frac{\lambda_{cr}}{L} \tag{54}$$

where L is the initial length of the SWCNT. Therefore, we can outline the compressive critical strains in table 2.

Agreeing Cao and Chen (2006), some scattering has been observed in the final critical strains depending of the increment size l_0 and the number of increments NI. Despite no explicit statistic analysis of this influence has been performed in this work, input data for compressive simulations are added in table 3 as guidance about their order of magnitude.

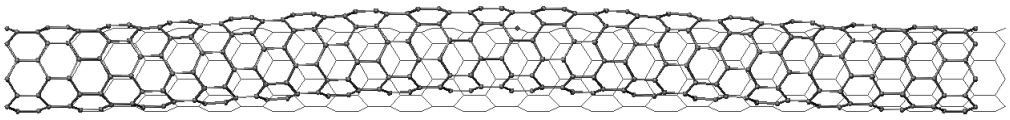

(a) ZigZag(7,0) AMBER

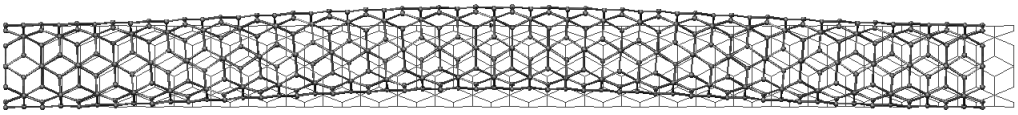

(b) Armchair(4,4) Morse

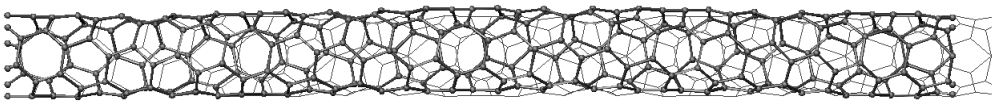

(c) Chiral(4,2) AMBER

(d) Chiral(4,2) Morse

Figure 8: Deformed shapes under compression (last increment)

		AMBER		MORSE	
	L(nm)	λ_{cr}(nm)	ε_{cr}(%)	λ_{cr}(nm)	ε_{cr}(%)
Armchair(3,3)	4.919	0.146	2.958	0.147	2.978
Armchair(4,4)	6.641	0.253	3.807	0.193	2.902
ZigZag(5,0)	4.757	0.306	6.426	0.132	2.783
ZigZag(7,0)	6.674	0.313	4.688	0.190	2.844
Chiral(4,2)	5.072	0.239	4.706	0.141	2.782
Chiral(5,3)	6.859	0.258	3.756	0.188	2.737

Table 2: Critical strains under compression

	AMBER		MORSE	
	l_0	NI	l_0	NI
Armchair(3,3)	0.05	65	0.05	65
Armchair(4,4)	0.1	30	0.1	39
ZigZag(5,0)	0.05	60	0.05	60
ZigZag(7,0)	0.1	40	0.1	40
Chiral(4,2)	0.05	75	0.05	75
Chiral(5,3)	0.02	200	0.05	74

Table 3: Input data in compressive simulations

Comparing values from table 2 can be seen that the comparison of values from table 2 shows that the adoption of different potential functions produces somewhat different values of λ_{cr}, although the order of magnitude of the final critical strains with both functions is similar. Thereby, we can conclude that the critical buckling is triggered before the constitutive nonlinearity takes place, according to Falvo et al. (1997); Iijima et al. (1996); Srivastava et al. (1999) and Y. Wang et al. (2005).

As can be seen, our results agree qualitatively well with other atomistic studies, mainly with MD simulations. For instance, Yakobson et al. (1996) obtained for a SWCNT of d =1 nm a critical compressive strain of 5%, Srivastava et al. (1999) obtained ε_{cr} = 8% and Ru (2000) estimated ε_{cr} = 7.5% for the same diameter. Likewise, Zhang et al. (2007, table 4) and Cornwell and Wille (1997) predicted for Armchair nanotubes the critical strains outlined in table 4, which agree reasonably with our values from table 2.

Zhang et al. (2007)			Cornwell and Wille (1997)		
	d(nm)	ε_{cr}(%)		d(nm)	ε_{cr}(%)
Armchair(4,4)	0.542	6.570	Armchair(9,9)	1.250	5.200
Armchair(5,5)	0.678	7.764	Armchair(12,12)	1.664	4.400
Armchair(6,6)	0.814	7.068	Armchair(19,19)	2.632	3.200
Armchair(7,7)	0.949	6.271			

Table 4: Critical strains estimated by other MD methods

As well, Y. Wang et al. (2005, fig. 2) obtained almost the same values as Cornwell and Wille (1997) for the same diameter range. Regarding Molecular Mechanics framework, Cao and Chen (2006) estimated by using the commercial software Materials Studio an average critical strain $\overline{\varepsilon}_{cr}$ = 6.6% for a ZigZag(9,0) SWCNT of 5.3 nm in length and $\overline{\varepsilon}_{cr}$ = 7.6% for an Armchair(5,5) SWCNT of 4.7 nm in length. Also Chang et al. (2005) yielded ε_{cr} = 10.7% for an Armchair(7,7) and ε_{cr} = 6.9% for an Armchair(10,10) nanotube, by a MM-based technique which minimizes the total potential energy. All of these values are in the range of our results in table 2 from the MSM model.

A controversial issue, extensively treated in several references (Cao and Chen, 2006; Chang et al., 2005; Odegard et al., 2002; Yakobson et al., 1996) is the applicability of the continuum models to predict the critical strains of compressed SWCNTs. According to Cao and Chen (2006), the presence of geometrical imperfections in the atomic structure (not explicitly represented in continuum models) affects the critical buckling strain of SWCNTs. Then, continuum models are not recommendable to tackle the geometrical nonlinear analysis of these nanostructures. Even if beam or shell-like models are supported with atomistic techniques (Chang et al., 2005) for validation, it is necessary to be cautious about the definition of some mechanical parameters.

Anyway, taking into account the aspect ratios from table 1 of our simulated SWCNTs under compression and the obtained deformed shapes in figure 8, a global buckling mode is yielded. Therefore, we could compare qualitatively our obtained critical strains with those obtained from Yakobson et al. (1996, eq. (2)) for global buckling failure mode (see table 5). Thus, a maximum relative shift of 20% is rendered.

	AMBER	MORSE	Yakobson et al. (1996)
	ε_{cr}(%)	ε_{cr}(%)	ε_{cr}(%)
Armchair(3,3)	2.958	2.978	3.375
Armchair(4,4)	2.876	2.902	3.292
ZigZag(5,0)	2.796	2.783	3.341
ZigZag(7,0)	2.836	2.844	3.327
Chiral(4,2)	2.780	2.782	3.293
Chiral(5,3)	2.727	2.737	3.150

Table 5: Comparison with Yakobson et al. (1996, eq. (2)) under compression

6.2. Flexural behavior

The nanotubes referenced in table 6 have been simulated under bending loads.

Chirality	d(nm)	L(nm)	L/d
Armchair(3,3)	0.407	1.230	3.02
Armchair(4,4)	0.542	1.722	3.17
ZigZag(5,0)	0.391	1.349	3.45
ZigZag(7,0)	0.548	1.775	3.24
Chiral(4,2)	0.414	1.240	2.99
Chiral(5,3)	0.548	1.789	3.26

Table 6: SWCNTs under bending

In this section, shorter nanotubes than those under compressive loads have been chosen, because we are focused on the analysis of the local buckling mode rather than the global one. A schematic description of the supporting conditions and prescribed displacements for the flexural behavior is displayed in figure 9.

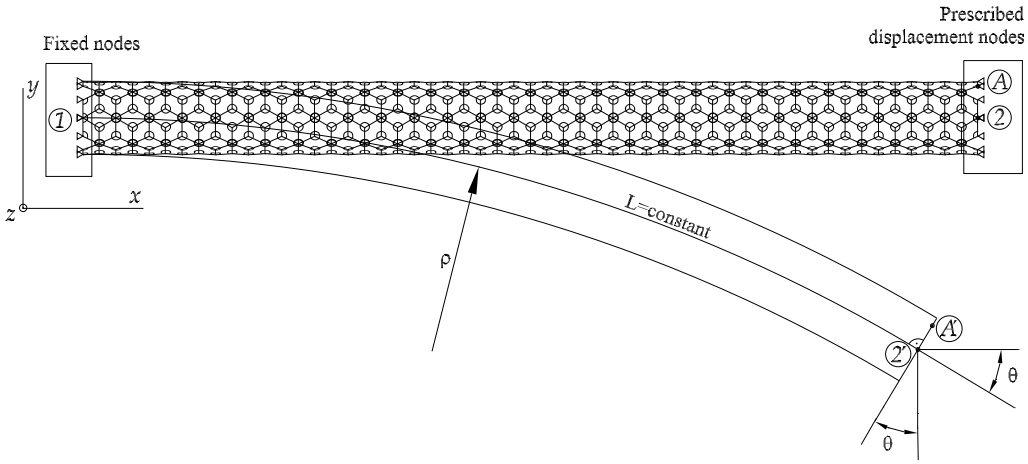

Figure 9: Supporting conditions under flexural loads

With regard to the possibilities of definition for the prescribed displacements $\Delta\overline{\mathbf{u}}$ at the right end of the SWCNT, we can classify them into two main groups:

1. The right end of the reference axis describes a known defined curve in the plane.
2. The right end traces a path such that the consecutive reference axis in the loading procedure constitute a family of known curves verifying a defined property.

In our case option 2 has been chosen, where the reference axis at a intermediate equilibrium position is supposed to be an arc of constant length. Moreover, the initial tangent of each arc is the neutral axis of the undeformed shape and the moving nodes at the right end verify a rigid body motion which keeps the cross-section orthogonal to the deformed reference axis along the loading process. In this way, the next relation is verified for each equilibrium configuration:

$$\rho\theta = L \tag{55}$$

Assuming the same coordinate system defined in section 6.1 and adopting the load factor for bending response as

$\lambda = \theta$, the displacements of the right end centre may be expressed for the first increment as:

$$\Delta\overline{u}_1^2 = -(L - \rho \sin \Delta\lambda_1) = -L\left(1 - \frac{\sin \Delta\lambda_1}{\Delta\lambda_1}\right) \tag{56a}$$

$$\Delta\overline{v}_1^2 = -\rho(1 - \cos \Delta\lambda_1) = -\frac{L}{\Delta\lambda_1}(1 - \cos \Delta\lambda_1) \tag{56b}$$

$$\Delta\overline{w}_1^2 = 0 \tag{56c}$$

Taking a generic node (node A) at the right end of the nanotube, the imposed displacements are written:

$$\Delta\overline{u}_1^A = \Delta\overline{u}_1^2 + y_A \sin \Delta\lambda_1 = -L\left(1 - \frac{\sin \Delta\lambda_1}{\Delta\lambda_1}\right) + y_A \sin \Delta\lambda_1 \tag{57a}$$

$$\Delta\overline{v}_1^A = \Delta\overline{v}_1^2 + y_A \cos \Delta\lambda_1 = -\left(\frac{L}{\Delta\lambda_1} + y_A\right)(1 - \cos \Delta\lambda_1) \tag{57b}$$

$$\Delta\overline{w}_1^A = \Delta\overline{w}_1^2 \tag{57c}$$

then, regarding $\Delta\lambda_n$ is small enough, eqs. (57) can be simplified as:

$$\begin{Bmatrix} \Delta\overline{u}_1^A \\ \Delta\overline{v}_1^A \\ \Delta\overline{w}_1^A \end{Bmatrix} = \Delta\lambda_1 \begin{Bmatrix} y_A \\ -L/2 \\ 0 \end{Bmatrix}$$

$$\Delta\overline{\mathbf{u}}_1^A = \Delta\lambda_1 \widetilde{\mathbf{u}}_1^A \tag{58}$$

For the following increments, the prescribed displacements at the right end can be determined by using eqs. (56) at the beginning and the end of the increment. Therefore, subtracting the resultant expressions we can reach:

$$\Delta\overline{u}_n^2 = \overline{u}_{n+1}^2 - \overline{u}_n^2 = L\left[\frac{\sin \lambda_{n+1}}{\lambda_{n+1}} - \frac{\sin \lambda_n}{\lambda_n}\right] \tag{59a}$$

$$\Delta\overline{v}_n^2 = \overline{v}_{n+1}^2 - \overline{v}_n^2 = -L\left[\frac{1 - \cos \lambda_{n+1}}{\lambda_{n+1}} - \frac{1 - \cos \lambda_n}{\lambda_n}\right] \tag{59b}$$

$$\Delta\overline{w}_n^2 = \overline{w}_{n+1}^2 - \overline{w}_n^2 = 0 \tag{59c}$$

In the same way, we can add the incremental displacements of the node A to equation (59) achieving:

$$\Delta\overline{u}_n^A = \Delta\overline{u}_n^2 + y_A(\sin \lambda_{n+1} - \sin \lambda_n) \tag{60a}$$

$$\Delta\overline{v}_n^A = \Delta\overline{v}_n^2 + y_A(\cos \lambda_{n+1} - \cos \lambda_n) \tag{60b}$$

$$\Delta\overline{w}_n^A = \Delta\overline{w}_n^2 \tag{60c}$$

After a few manipulations and assuming $\Delta\lambda_n$ is small enough, the next simplified expressions for the imposed displacements at the node A are obtained:

$$\begin{Bmatrix} \Delta\overline{u}_n^A \\ \Delta\overline{v}_n^A \\ \Delta\overline{w}_n^A \end{Bmatrix} = \Delta\lambda_n \begin{Bmatrix} \frac{L}{\lambda_n}\left(\cos \lambda_n - \frac{\sin \lambda_n}{\lambda_n}\right) + y_A \cos \lambda_n \\ \frac{L}{\lambda_n}\left(\frac{1-\cos \lambda_n}{\lambda_n} - \sin \lambda_n\right) - y_A \sin \lambda_n \\ 0 \end{Bmatrix}$$

$$\Delta\overline{\mathbf{u}}_n^A = \Delta\lambda_n \widetilde{\mathbf{u}}_n^A \tag{61}$$

The prescribed displacements are updated only in the predictive phase, leading to a *redistribution of internal forces* in the corrective one, up to reach the next equilibrium configuration. Hence, superscript k disappears from eq. (56) to eq. (61).

Some obtained nonlinear equilibrium paths under bending and their deformed shapes at the last iteration (of the last increment) are provided in figures 10 and 11 respectively, as an example of the buckling behavior. The

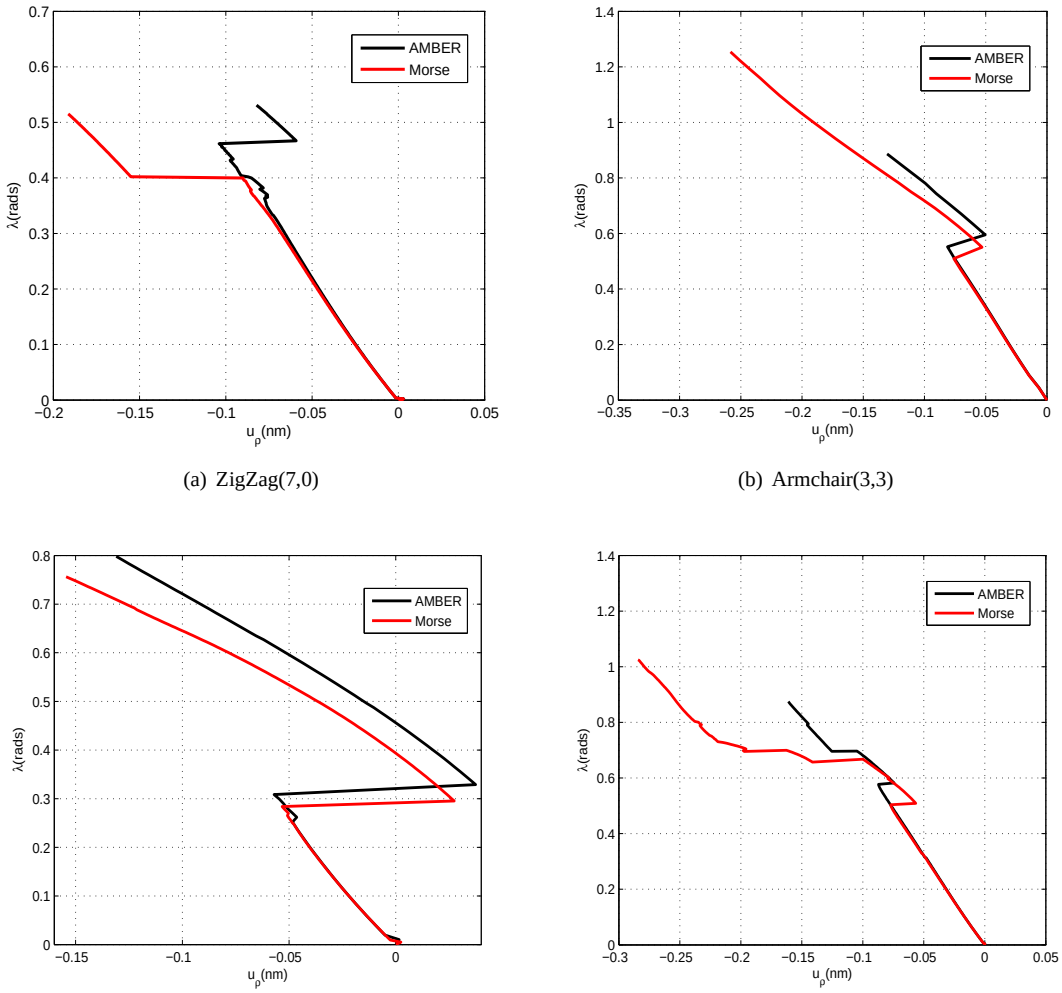

(a) ZigZag(7,0)

(b) Armchair(3,3)

(c) Armchair(4,4)

(d) Chiral(4,2)

Figure 10: Nonlinear equilibrium paths under bending (color on the Web)

transversal displacement of a representative node u_ρ around the midpoint at the compressed side of the nanotube has been represented against the load factor λ.

Initial imperfections in bending simulations have been adopted as a point load in the y-axis direction at a node near the midpoint of the compressed (bottom) side of the SWCNT, testing out their values trying to reproduce a clear post-critical behavior without divergence of the numerical process (see section 6.4).

For each critical load factor (right end rotation), the buckling curvature can be obtained from (55) as:

$$\kappa_{cr} = \frac{\lambda_{cr}}{L} \tag{62}$$

Note that equation (62) is an approximation to the real buckling curvature because the right-end rotation $\lambda = \theta$ is not necessarily the same as the rotation of the cross-section corresponding to the buckling point. Although the ideal reference axis is an arc of circumference with constant θ, the *redistribution* of the corrective phase into each increment introduces an accumulative deviation from this curve.

The critical buckling curvatures (in nm^{-1}) in table 7 have been obtained extracting λ_{cr} from each equilibrium

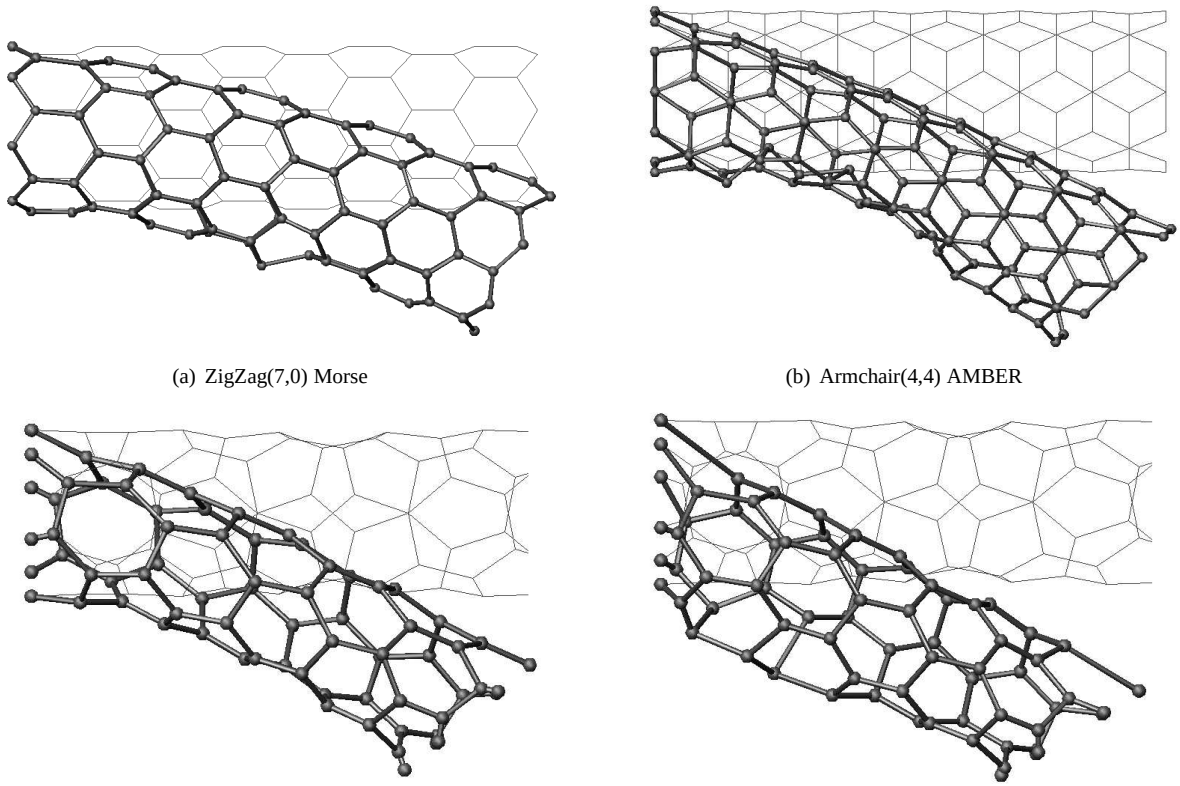

(a) ZigZag(7,0) Morse

(b) Armchair(4,4) AMBER

(c) Chiral(4,2) AMBER

(d) Chiral(4,2) Morse

Figure 11: Deformed shapes under bending (last iteration)

path. In some cases (fig. 10(a), AMBER potential and fig. 10(d)), it is difficult to find out the buckling step which determines λ_{cr}. In this case, the first abrupt shift into each curve has been taken as the corresponding critical strain, interpreting the rest of deviations as numerical singularities. This choice may be open to misinterpretation and a previous contrast of results with different input data for each simulation has been found useful (see section 6.4).

In addition, we can see an abrupt change of direction in the u_ρ displacement (figure 10(a)) for AMBER potential compared with Morse function. In order to clarify the origin of this phenomenon, the final deformed shape and some equilibrium paths of additional nodes for ZigZag(7,0) with AMBER potential were studied (figure 12). Particularly, the node 74 was monitored in figure 10(a) and equilibrium paths of the nodes located at the same cross-section of the nanotube are plotted in figure 12(b). Taking into account the symmetry of the SWNT with respect to a vertical plane containing the reference axis, each couple of nodes denoted in figure 12(a) rendered the same equilibrium path. As can be seen, the gap into the equilibrium path of node 74 is a local singularity that does not appear in the rest of nodes. Therefore, it can be associated with a local *snap-through* phenomenon, which is dispersed before reaching neighboring nodes. A similar situation occurs in the compressed side near the left end of the nanotube (see figure 12(a)).

The control node should be chosen carefully because nodes located far from the instability generate curves with small kinks or without them. Therefore, some tests of the same SWCNT monitoring different nodes were necessary into each simulation in order to choose the most suitable control node. However, provided a set of nodes that yield curves where the buckling gap is present, the value of λ_{cr} is independent of the choice of the node.

As we did in compression, input data for flexural simulations are included in table 8 as guidance about their order of magnitude.

As can be seen from figure 10 and comparing values from table 7, each interatomic potential produces different

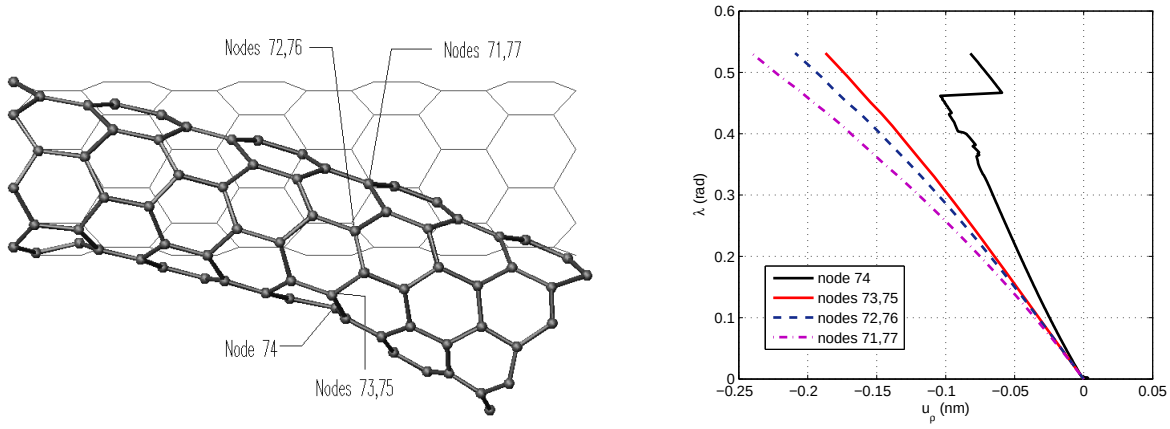

(a) ZigZag(7,0) deformed shape

(b) Equilibrium paths (color on the Web)

Figure 12: ZigZag(7,0) with AMBER potential revisited

		AMBER		MORSE	
	L(nm)	λ_{cr}(rad)	κ_{cr}(nm^{-1})	λ_{cr}(rad)	κ_{cr}(nm^{-1})
Armchair(3,3)	1.230	0.552	0.449	0.510	0.414
Armchair(4,4)	1.722	0.308	0.179	0.284	0.165
ZigZag(5,0)	1.349	1.148	0.851	0.636	0.472
ZigZag(7,0)	1.775	0.462	0.260	0.400	0.225
Chiral(4,2)	1.240	0.577	0.466	0.504	0.407
Chiral(5,3)	1.789	0.304	0.170	0.293	0.164

Table 7: Critical buckling curvatures under bending

	AMBER		MORSE	
	l_0	NI	l_0	NI
Armchair(3,3)	0.1	22	0.1	35
Armchair(4,4)	0.04	90	0.02	180
ZigZag(5,0)	0.1	34	0.1	19
ZigZag(7,0)	0.01	250	0.01	250
Chiral(4,2)	0.01	240	0.01	327
Chiral(5,3)	0.05	80	0.02	100

Table 8: Input data in flexural simulations

critical buckling curvature. Nevertheless, no clear systematic trend in terms of stiffness is observed. In fact, the constitutive differences due to the interatomic potential function are coupled with various effects as the scattering from the input data or the border effects (short simulated nanotubes).

Regarding the snapshots of deformed shapes in fig. 11, a kind of flattening of the cross-section of the nanotube can be qualitatively seen, as has been reported (Iijima et al., 1996; Wang et al., 2008; Yakobson et al., 1996). This resembles the so-called Brazier effect (Brazier, 1927) in continuum mechanics. Despite this effect appears mainly in cylindrical shells, in our atomistic MSM model it is also reproduced. However, in some cases (see fig. 11(d)) the final deformed shape is distorted by the border effects, which amplifies the instability near the SWCNT left end due to some strongly compressed bonds. The effect of the snap to secondary critical steps detected by the numerical procedure (fig.

10(d)) is present in these unusual deformed shapes. In fact, these special deformed shapes occur only after buckling. For instance, the Chiral(4,2) with Morse potential (fig. 11(d)) reaches a $\lambda_{cr} = 0.504$ rad in the increment $n = 133$ and running our code which uses Morse potential up to that increment, the deformed shape (figure 13) shows the expected smoothness in the compressed side.

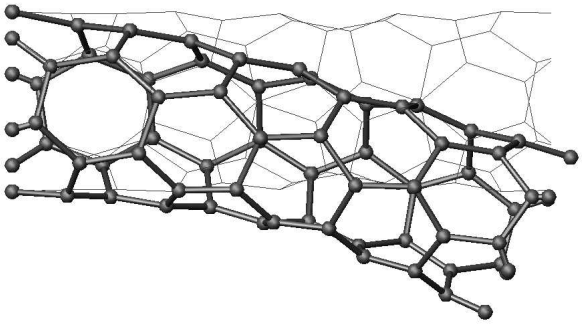

Figure 13: Chiral(4,2), Morse deformed shape, $n = 133$

Our results agree reasonably with other published references. For instance, Pantano et al. (2004) proposes a critical buckling rotation of $\theta_{cr} = 1.1$ rad for a ZigZag(13,0) nanotube of 2 nm in diameter and 8 nm in length through FE modeling validated with MD techniques. These values translate into a critical curvature of $\kappa_{cr} = 0.1375\,\text{nm}^{-1}$, slightly lower than our results for a higher diameter. Otherwise, Iijima et al. (1996) used MD calculations for a SWCNT of 1.2 nm in diameter obtaining a critical rotation of $\theta_{cr} = 30^{\text{o}} = 0.5236$ rad, closer to our obtained values in terms of magnitude order. Also in Iijima et al. (1996, eq. (2)) is introduced a numerical fitting to their own MD results for bending. However, it is limited to the diameter range of $[1, 1.5]$ nm and it is meaningless to be used herein.

Despite of using a cylindrical shell model (not recommendable) valuated with MD techniques, Yakobson et al. (1996, eq. (4)) estimate the critical curvatures in table 9 for our diameter range.

	d(nm)	L(nm)	$\kappa_{cr}(\text{nm}^{-1})$
Armchair(3,3)	0.407	1.230	0.937
Armchair(4,4)	0.542	1.722	0.527
ZigZag(5,0)	0.391	1.349	1.012
ZigZag(7,0)	0.548	1.775	0.516
Chiral(4,2)	0.414	1.240	0.903
Chiral(5,3)	0.548	1.789	0.516

Table 9: Estimated critical buckling curvatures under bending (Yakobson et al., 1996, eq. (4))

These values are reasonably close to those presented in this work (see table 7).

6.3. Torsional behavior

The dimensions and chiralities of the SWCNTs simulated under torsion are outlined in table 10.

A schematic description of the supporting conditions and the system of imposed displacements is depicted in figure 14. In this loading case, the right end nodes verify a rigid body rotation $\theta = \lambda$ in the positive x direction.

In order to simplify the development of the expressions which provide the prescribed displacements of a generic right end node A in terms of the load factor, we assume initially that the increments $\Delta\lambda_n,\ n = 1, 2, \ldots, NI$ are small enough. Therefore, $\Delta\lambda_n \ll \lambda_n$ and $\Delta\lambda_n \ll \theta_0$ (see figs 14(b) and 14(c)). For the first increment, we have:

$$|\Delta\overline{\mathbf{u}}_1^A| \simeq R\Delta\lambda_1 \tag{63}$$

Chirality	d(nm)	L(nm)	L/d
Armchair(3,3)	0.407	1.476	3.63
Armchair(4,4)	0.542	1.968	3.63
ZigZag(5,0)	0.391	1.562	3.99
ZigZag(7,0)	0.548	1.988	3.63
Chiral(4,2)	0.414	1.465	3.54
Chiral(5,3)	0.548	2.028	3.70

Table 10: SWCNTs under torsion

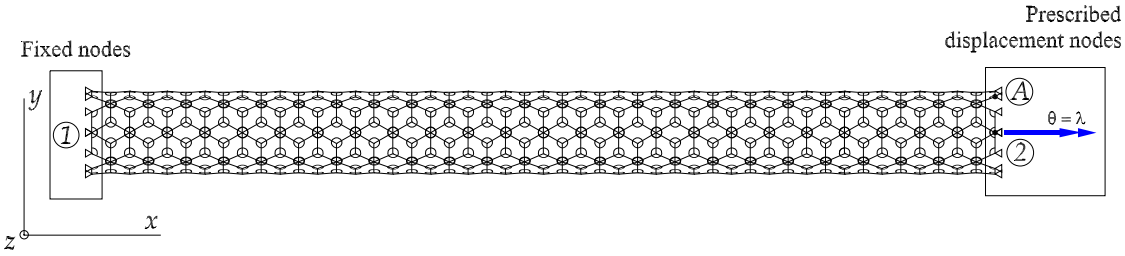

(a) Supporting conditions under torsion

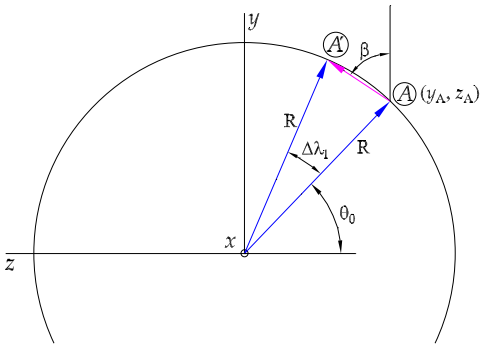

(b) Rotation first increment

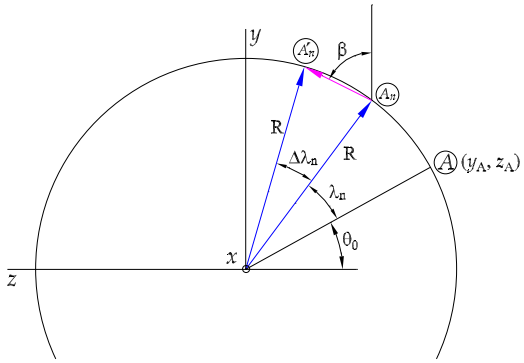

(c) Rotation generic increment

Figure 14: Supporting conditions and imposed displacements schemes (color on the Web)

projecting onto the coordinate axes:

$$\Delta\overline{u}_1^A = 0 \tag{64a}$$

$$\Delta\overline{v}_1^A = \Delta\lambda_1 R\cos\beta \tag{64b}$$

$$\Delta\overline{w}_1^A = \Delta\lambda_1 R\sin\beta \tag{64c}$$

Since $\beta \simeq \theta_0$, equation (64) becomes:

$$\begin{Bmatrix} \Delta\overline{u}_1^A \\ \Delta\overline{v}_1^A \\ \Delta\overline{w}_1^A \end{Bmatrix} = \Delta\lambda_1 \begin{Bmatrix} 0 \\ -z_A \\ y_A \end{Bmatrix}$$

$$\Delta\overline{\mathbf{u}}_1^A = \Delta\lambda_1 \widetilde{\mathbf{u}}_1^A \tag{65}$$

For the subsequent increments (fig 14(c)), expressions (64) adopt the form:

$$\Delta\overline{u}_n^A = 0 \tag{66a}$$

$$\Delta\overline{v}_n^A = \Delta\lambda_n R\cos\beta \tag{66b}$$

$$\Delta\overline{w}_n^A = \Delta\lambda_n R\sin\beta \tag{66c}$$

Since $\beta \simeq \theta_0 + \lambda_n$, eqs. (66) can be rewritten:

$$\begin{Bmatrix} \Delta\overline{u}_n^A \\ \Delta\overline{v}_n^A \\ \Delta\overline{w}_n^A \end{Bmatrix} = \Delta\lambda_n \begin{Bmatrix} 0 \\ -z_A\cos\lambda_n - y_A\sin\lambda_n \\ y_A\cos\lambda_n - z_A\sin\lambda_n \end{Bmatrix}$$

$$\Delta\overline{\mathbf{u}}_n^A = \Delta\lambda_n \widetilde{\mathbf{u}}_n^A \tag{67}$$

As we did in sections 6.1 and 6.2, the imposed displacements are updated only in the predictive phase.

Several nonlinear equilibrium paths under torsion and their final deformed shapes are displayed in figures 15 and 16 respectively, as examples of the local buckling under torsional loads. The transversal displacement u_ρ of a representative node around the midpoint of the nanotube has been plotted against the load factor λ.

Initial imperfections in torsional simulations have been introduced through two point loads in the y-axis direction and opposite senses, either stretching or flattening the cross-section of the tube. Their values have been tested out trying to reproduce reasonably the post-buckling behavior without divergence of the numerical process (see section 6.4).

Values in table 11 are obtained extracting the critical rotation of the right end (equivalent to λ_{cr}) from each equilibrium path, in the same way it has been done in bending. As has been aforementioned, this choice may be controversial. In torsion, the first abrupt shift into each curve has been taken as the corresponding critical strain, assigning the rest of deviations to numerical singularities.

As we did in compression, input data for flexural simulations are included in table 8 as guidance about their order of magnitude.

As we did in compression and bending, input data of torsional simulations are included in table 12 to give an idea of their order of magnitude.

	AMBER	MORSE	Yakobson et al. (1996, eq. (6))
	λ_{cr}(rad)	λ_{cr}(rad)	λ_{cr}(rad)
Armchair(3,3)	0.865	0.971	0.180
Armchair(4,4)	0.694	0.653	0.117
ZigZag(5,0)	0.958	1.162	0.210
ZigZag(7,0)	0.706	0.831	0.115
Chiral(4,2)	1.000	0.718	0.171
Chiral(5,3)	0.783	0.766	0.118

Table 11: Critical buckling rotations under torsion

Comparing values from table 11 and equilibrium paths from figure 15 can be stated that there is not a clear tendency in λ_{cr} by taking AMBER or Morse potential into account. Therefore, we can conclude that the interatomic potential does not produce any difference related to the critical buckling strains.

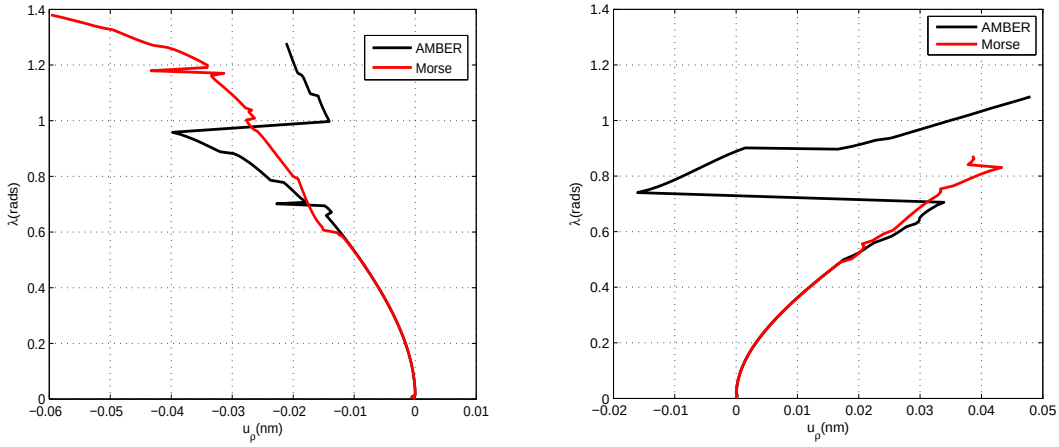

(a) ZigZag(5,0) (b) ZigZag(7,0)

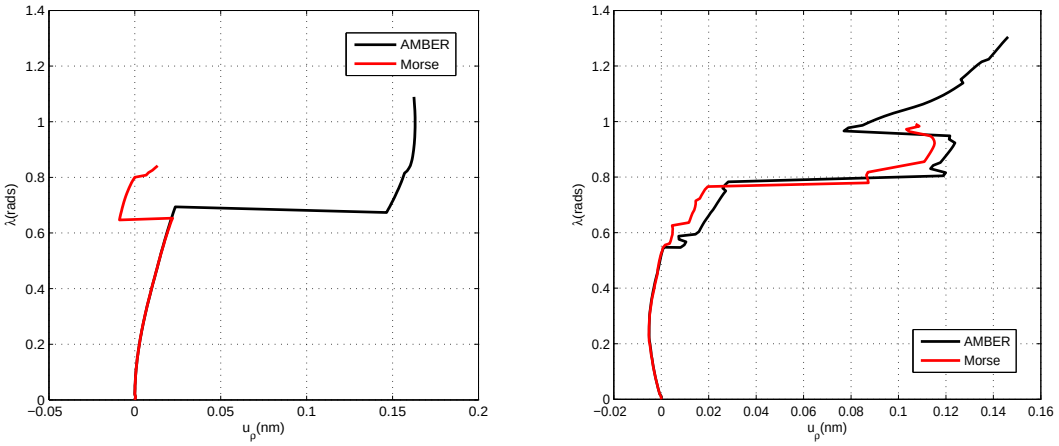

(c) Armchair(4,4) (d) Chiral(5,3)

Figure 15: Nonlinear equilibrium paths under torsion (color on the Web)

	AMBER		MORSE	
	l_0	NI	l_0	NI
Armchair(3,3)	0.01	164	0.01	185
Armchair(4,4)	0.02	100	0.02	80
ZigZag(5,0)	0.01	160	0.01	175
ZigZag(7,0)	0.02	100	0.02	80
Chiral(4,2)	0.01	180	0.01	160
Chiral(5,3)	0.02	120	0.02	92

Table 12: Input data in torsional simulations

The failure mechanism under torsion leads to a flattening of the cross section in a helix-like deformed shape (see fig 16), as has been previously reported by Rochefort et al. (1999, fig. 6), Yakobson et al. (1996, fig. 4) and Wang et al.

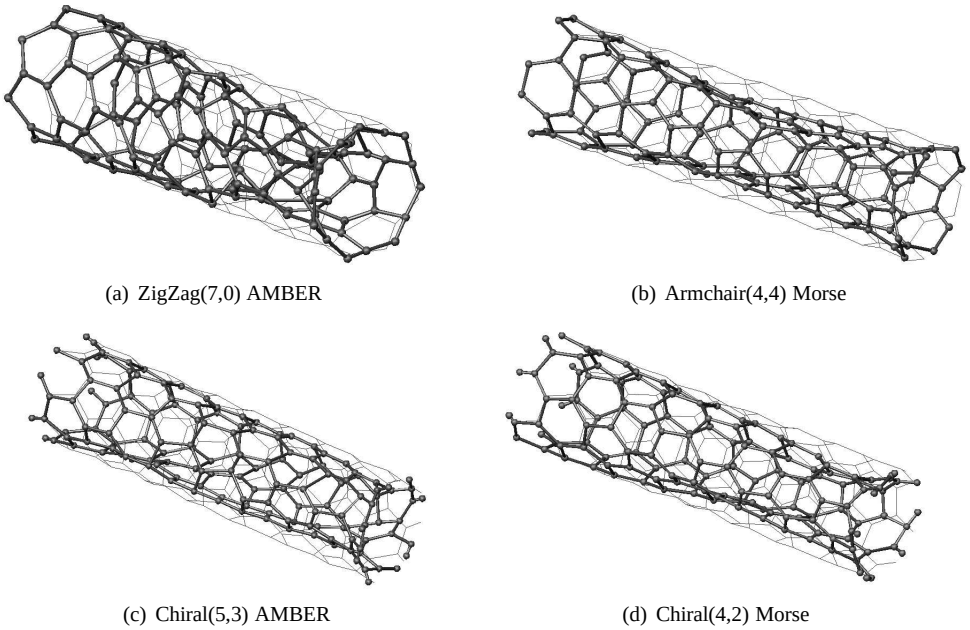

(a) ZigZag(7,0) AMBER (b) Armchair(4,4) Morse

(c) Chiral(5,3) AMBER (d) Chiral(4,2) Morse

Figure 16: Final deformed shapes under torsion

(2004, fig. 4).

Regarding the critical buckling rotations, Yakobson et al. (1996) reported λ_{cr} =2.7 rad for a ZigZag(13,0) SWCNT of 1 nm in diameter and 23 nm in length, which is comparable with our obtained results in table 11. Furthermore, in the same work a validation of their own MD calculations by means of continuum models has been established under torsional loads. Namely, if $L \leq 136\ d^{5/2}$ (short cylinders) which can be easily verified in our case, eq. (6) from Yakobson et al. (1996) provide the results shown in the last column of table 11. Of course their values are quite lower than ours because the tubes simulated in this work under torsion are rather short and the circumferential constraints produced by the pinned joints at both ends tend to keep the circular cross-section and stabilize the whole structure against torsional buckling.

6.4. Estimation of error and reliability of the method

In order to give an idea about the influence of the input data ($l_0, NI, \boldsymbol{\epsilon}$), a set of results under different values of these parameters is provided in this section. Despite no analytical or numerical optimization procedure has been carried out, the reliability of the numerical method against the variation of the input data is shown here. Note that all provided tests have been worked out with AMBER potential, because of the limited stability of the results obtained with the Morse function due to its nonlinear nature (see eqs. (44)). In fact, with the latter potential, only a few combinations (mainly in bending and torsion) of initial imperfections and increment size produce reasonable results once the critical load factor is reached; some of them were included in figs. 10 and 15.

Firstly, the influence of the increment size l_0 in the equilibrium paths under compression, bending and torsion has been investigated. One of the previously simulated nanotubes has been used as a reference for each loading distribution. The values of l_0 are bounded into an interval depending of the particular conditions of the algorithm (see Felippa (2001, Sec.18.2)). For instance, with $l_0 = 0.2$ all tests diverged before observing any kink in the corresponding curve. Therefore, a set of three representative values for each SWCNT were tested to study its final response, but keeping the initial imperfections as constant values. The final values of λ_{cr} (extracted from the first abrupt change of direction in the corresponding nonlinear path) are outlined in table 13, and the equilibrium paths in figure 17.

The procedure is quite reliable in compression and bending regarding the increment size, presenting relative errors in λ_{cr} (with respect to the minimum values) of 0.2% and 6% respectively. However, a relative error of nearly 30% is observed due to the $\lambda_{cr} = 0.8992$ rad for $l_0 = 0.1$. Nevertheless, from figure 17(c) substantial instabilities can be

Armchair(3,3) compression $d = 0.407$ nm, $L = 4.919$ nm			Armchair(4,4) bending $d = 0.542$ nm, $L = 1.722$ nm			ZigZag(7,0) torsion $d = 0.548$ nm, $L = 1.988$ nm		
l_0	NI	λ_{cr}(nm)	l_0	NI	λ_{cr}(rad)	l_0	NI	λ_{cr}(rad)
0.1	30	0.1456	0.1	20	0.2904	0.1	20	0.8992
0.05	65	0.1455	0.04	90	0.3083	0.02	100	0.7055
0.01	300	0.1458	0.02	127	0.3034	0.01	200	0.6948

Table 13: λ_{cr} against increment size l_0

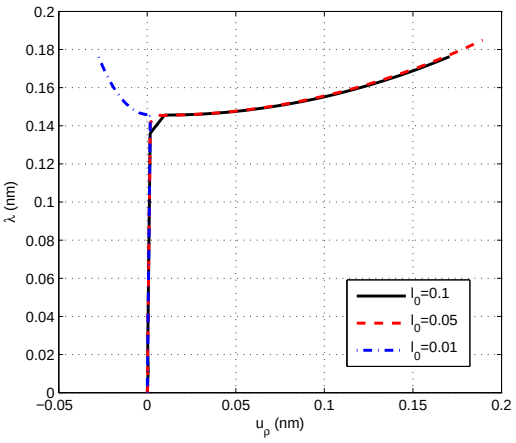

(a) Armchair(3,3) compression

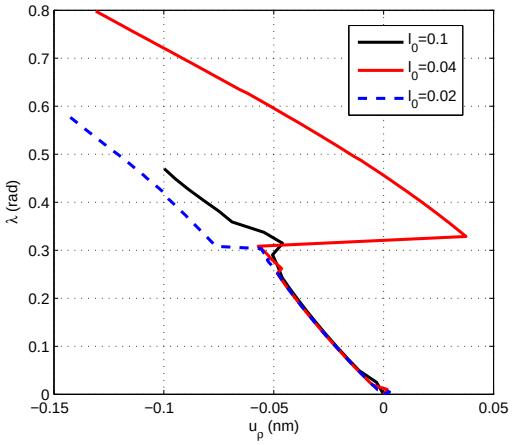

(b) Armchair(4,4) bending

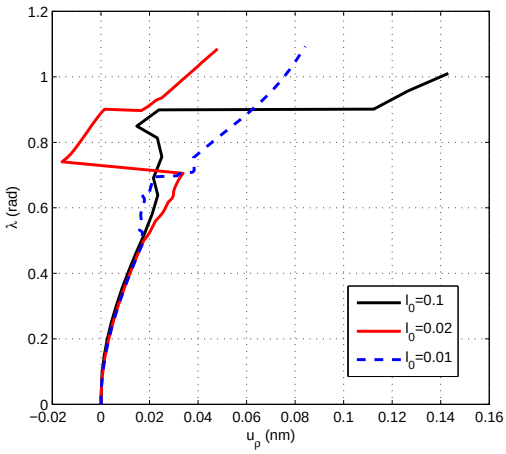

(c) ZigZag(7,0) torsion

Figure 17: Equilibrium paths with different increment size l_0 (color on the Web)

seen in the corresponding curve around $\lambda_{cr} = 0.7$, which is the load factor detected in the other two curves. It is also remarkable that in some of the tested nanotube configurations, certain values of l_0 introduce a different direction of the displacement after the buckling point. Namely, taking a value of $l_0 = 0.01$ in compression (figure 17(a)) a completely reverse direction of the displacement has been rendered, which can be attributed to a global *snap-through*

phenomenon. Likewise, in figures 17(b) and 17(c), the change in direction of certain curves can be interpreted as a local *snap-through* phenomenon limited to a few nodes.

Next, the influence of initial imperfections is studied by keeping the increment size as a constant value and giving three representative values to these perturbations. The final values of λ_{cr} are outlined in table 14, and the equilibrium paths in figure 18.

Armchair(3,3) compr. $d = 0.407$ nm $L = 4.919$ nm		Armchair(4,4) bend. $d = 0.542$ nm $L = 1.722$ nm		ZigZag(7,0) tors. $d = 0.548$ nm $L = 1.988$ nm	
ϵ (nN/nm)	λ_{cr} (nm)	ϵ (nN)	λ_{cr} (rad)	ϵ (nN)	λ_{cr} (rad)
6x0.01	0.1457	1x1	0.3180	2x0.05	0.6974
6x0.1	0.1455	1x10	0.3083	2x0.5	0.7055
6x1	0.1455	1x100	0.3954	2x5	0.6413

Table 14: λ_{cr} against initial imperfections ϵ

Regarding the distribution of initial imperfections, in compression six point loads have been applied on the nodes located at the midsection of the nanotube, in bending a point load has been applied on the node located around the midsection of the SWCNT at the compressed (bottom) side and in torsion two opposite loads have been applied at the midsection of the nanotube which tend to flatten the cross section. Although a previous understanding of the load configuration is needed to choose a reasonable distribution, some additional tests locating the set of loads which introduces initial perturbations at $\simeq L/4$ from the right end were performed. For instance, applying six imperfections of 0.1 nN/nm under compression, an imperfection of 10 nN under bending and two opposite imperfections of 0.5 nN under torsion, respective values of $\lambda_{cr} = 0.1457$ nm, $\lambda_{cr} = 0.3901$ rad and $\lambda_{cr} = 0.7061$ rad were obtained. Comparing these critical load factors with the corresponding values in table 14, can be seen that no important differences have been yielded by changing the distribution of initial imperfections. Nonetheless, placing initial imperfections at $\simeq L/4$ from the right end causes an earlier divergent behavior of the numerical algorithm than placing imperfections at the midsection.

As we can see in table 14, the critical load factor is reasonably stable related to the variation of the values of the perturbation ϵ, presenting relative errors (with respect to the minimum obtained value) of 0.15% in compression, 30% in bending and 10% in torsion. Figure 18(b) shows that the rough imperfection of 100 nN renders a meaningless equilibrium path, the load factor of which increases the relative error in bending.

To sum up, the input data (l_0, NI and ϵ) adopted to obtain the equilibrium paths presented from section 6.1 to 6.3 were selected in order to discard numerical instabilities attending to criteria of smoothness of the curve, clarity in the main abrupt kink (interpreted as λ_{cr}) and longest curve after buckling.

7. Concluding remarks

In this paper, a geometrical nonlinear extension of the general formulation for the 'stick-spiral' model has been presented. Calculations with both AMBER and Morse potential functions have been carried out, focused on checking wether the buckling failure is triggered in the linear range of strains. The versatility of our formulation is highlighted by its ability of considering general load conditions without additional equations even in geometrical nonlinear analysis, against other published works (Chang et al., 2005). As examples of this issue, compressive, flexural and torsional load configurations were adopted. Moreover, a set of clamped-clamped like tubes have been loaded in each case through imposed displacements at the moving nodes of their right end. Likewise, two incremental-iterative procedures (regarding AMBER or Morse potentials) involving a general arc-length control strategy have been developed and numerically implemented. Hence, nonlinear equilibrium paths, critical buckling strains and final deformed shapes have been presented as output results and compared with other published works.

To sum up, the main conclusions of this study are detailed next:

1. Related to the critical strains values under compression (see table 2), utilizing either Morse or AMBER potential in the calculations does not produce a clear difference. Likewise, despite of somehow different values are obtained

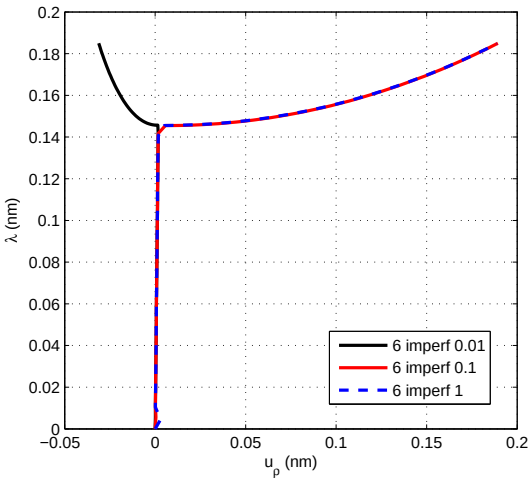

(a) Armchair(3,3) compression

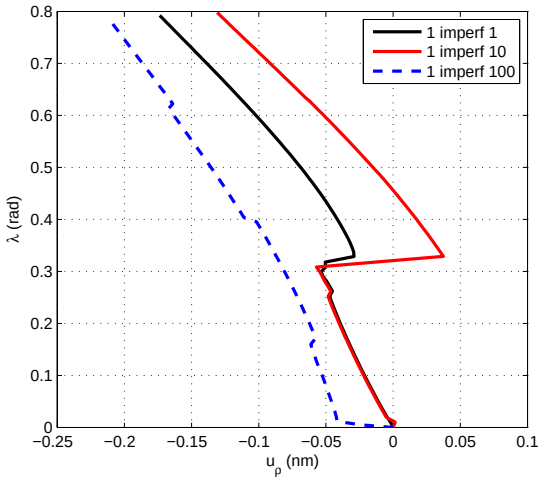

(b) Armchair(4,4) bending

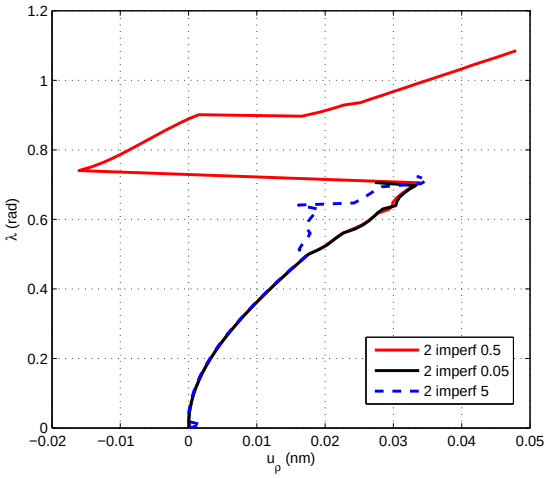

(c) ZigZag(7,0) torsion

Figure 18: Equilibrium paths with different imperfections ϵ (color on the Web)

under bending or torsion (tables 7 and 11), no clear trend has been observed. Therefore, we can conclude that the constitutive nonlinearity introduced by the Morse potential does not have a significant influence on the buckling response regarding the order of magnitude of the obtained critical strains. In this way, the geometrical instability of SWCNTs is triggered previously to their constitutive nonlinearity, agreeing with Falvo et al. (1997); Iijima et al. (1996); Srivastava et al. (1999) and Y. Wang et al. (2005).

2. The atomistic calculations developed in this paper emphasize that continuum models are not recommendable for the geometrically nonlinear analysis of SWCNTs. Besides the controversial choice of some parameters as the Young modulus, the equivalent wall thickness and/or the shear deformation (in beam models), continuum models cannot reproduce the atomistic structure of nanotubes. In fact, our atomistic MSM model allows to introduce directly geometrical imperfections (highly determining in the buckling behavior), constituting a great advantage in contrast with continuum models. In the latter case, these imperfections are included indirectly by means of contrived methods, which translates into a great loss of accuracy and unrealistic results.

3. As has been shown, our results are reasonable in comparison to those from previous atomistic works (e.g. Iijima et al., 1996; Srivastava et al., 1999; Wang et al., 2004; Zhang et al., 2007). On the other hand, despite the application of continuum models to atomistic systems is not advisable, some authors (Yakobson et al., 1996) have used them by taking the proper values for some mechanical parameters to validate their atomistic MD calculations. Thereby, we have used some of their continuum equations to compare with our results, rendering a reasonable agreement in compression (maximum relative error about 20%). Nevertheless, just a qualitative agreement in terms of order of magnitude under bending and torsion is obtained.
4. As output of our developed codes, nonlinear equilibrium paths are rendered. Deformed shapes, bond axial forces, angular moments and joint reactions at the last iteration of the last increment have been obtained. Regarding the values of buckling strains and the final deformed shapes, the differences with respect to other researches are mainly due to:
   i. The relatively small size of our simulated results
   ii. The border effects caused by the circumferential constraints at both ends
   iii. The implicit scattering produced by the input data of the incremental-iterative procedure into the critical buckling strains (Cao and Chen, 2006).

References

Ajayan, P., Schadler, L., Giannaris, C., Rubio, A., 2000. Single-walled carbon nanotube-polymer composites: Strength and weakness. Advanced Materials 12, 750-753.

Arroyo, M., Belytschko, T., 2003. Nonlinear mechanical response and rippling of thick multiwalled carbon nanotubes. Phys. Rev. Lett. 91, 215505-215508.

Belytschko, T., Xiao, S.P., Schatz, G.C., Ruoff, R.S., 2002. Atomistic simulations of nanotube fracture. Phys. Rev. B 65, 235430-235437.

Brazier, L.G., 1927. On the flexure of thin cylidrical shells and other "thin" sections. Proc. Royal Society London A 116, 104-114.

Brenner, D.W., 1990. Empirical potential for hydrocarbons for use in simulating the chemical vapor deposition of diamond films. Phys. Rev. B 42, 9458-9471.

Cao, G., Chen, X., 2006. The effect of the displacement increment on the axial compressive buckling behaviours of single-walled carbon nanotubes. Nanotechnology 17, 3844-3855.

Chang, T., Gao, H., 2003. Size-dependent elastic properties of a single-walled carbon nanotube via a molecular mechanics model. J. Mech. Phys. Solids 51, 1059-1074.

Chang, T., Li, G., Guo, X., 2005. Elastic axial buckling of carbon nanotubes via a molecular mechanics model. Carbon 43, 287-294.

Chang, T., Geng, J., Guo, X., 2006. Prediction of chirality- and size-dependent elastic properties of single-walled carbon nanotubes via a molecular mechanics model. Proc. R. Soc. A 462, 2523-2540.

Cornwell, C.F., Wille, L.T., 1997. Elastic properties of single-walled carbon nanotubes in compression. Solid State Commun. 101, 555-558.

Dresselhaus, M.S., Dresselhaus, G., Avouris, P., 2001. Carbon Nanotubes: Synthesis, Structure, Properties, and Applications, Topics in Applied Physics (vol 80), Springer, Berlin.

Falvo, M.R., Clary, G.J., Taylor, R.M., Chi, V., Brooks, F.P., Washburn, S., Superfine, R., 1997. Bending and buckling of carbon nanotubes under large strain. Nature 389, 582-584.

Felippa, C.A., 2001. Nonlinear Finite Element Method. Notes for a graduate course offered at the University of Colorado, Boulder. http://www.colorado.edu/engineering/Aerospace/CAS/courses.d/NFEM.d. Last accessed: October 26^{th}, 2013.

Hernández, E., Goze, C., Bernier, P., Rubio, A., 1998. Elastic properties of C and $B_xC_yN_z$ composite Nanotubes. Phys. Rev. Lett. 80, 4502–4505.

Iijima, S., Brabec, C., Maiti, A., Bernhol, J., 1996. Structural flexibility of carbon nanotubes. J. Chem. Phys. 104, 2089-2092.

Kang, I., Schulz, M.J., Kim, J.H., Shanov, V., Shi, D., 2006. A carbon nanotube strain sensor for structural health monitoring. Smart Materials and Structures 15, 737-748.

Lanczos, C., 1986. The Variational Principles of Mechanics, Dover, New York.

Lau, K.T., Chipara, M., Ling, H.Y., Hui, D., 2004. On the effective elastic moduli of carbon nanotubes for nanocomposite structures. Compos. Part B: Eng. 35, 95-101.

Li, C., Chou, T.W., 2003. A structural mechanics approach for the analysis of carbon nanotubes. Int. J. Solids Struct. 40, 2487-2499.

Li, C., Chou, T.W., 2003. Elastic moduli of multi-walled carbon nanotubes and the effect of van der waals forces. Compos. Sci. Technol. 63, 1517-1524.

Li, X., Yang, W., Liu, B., 2007. Bending Induced Rippling and Twisting of Multiwalled Carbon Nanotubes. Phys. Rev. Lett. 98, 205502-205505.

Liu, J.Z., Zheng, Q., Jiang, Q., 2003. Effect of bending instabilities on the measurements of mechanical properties of multiwalled carbon nanotubes. Phys. Rev. B 67, 075414-075421.

Malvern, L.E., 1969. Introduction to the mechanics of a continuous medium, Prentice Hall, Englewood Cliffs N. Jersey.

Meo, M., Rossi, M., 2006. Prediction of young's modulus of single wall carbon nanotubes by molecular-mechanics based finite element modelling. Compos. Sci. Technol. 66, 1597-1605.

Merli, R., Lázaro, C., Monleón, S., Domingo, A., 2013. A Molecular Structural Mechanics model applied to the static behavior of single-walled Carbon nanotubes: New general formulation. Comput. & Struct. 127, 68-87.

Naieni, A.K., Yaghoobi, P., Nojeh, A., 2011. Structural deformations and current oscillations in armchair-carbon nanotube cross devices: a theoretical study. J. Phys. D: Appl. Phys. 44, 085402-085408.

Natsuki, T., Tantrakarn, K., Endo, M., 2004. Prediction of elastic properties for singlewalled carbon nanotubes. Carbon 42, 39-45.
Natsuki, T., Endo, M., 2004. Stress simulation of carbon nanotubes in tension and compression. Carbon 42, 2147-2151.
Odegard, G.M., Gates, T.S., Nicholson, L.M., Wise, K.E., 2002. Equivalent-continuum modeling of nano-structured materials. Compos. Sci. Technol. 62, 1869-1880.
Pantano, A., Parks, D.M., Boyce, M.C., 2004. Mechanics of deformation of single- and multi-wall carbon nanotubes. J. Mech. Phys. Solids 52, 789–821.
Parnes, R., Chiskis, A., 2002. Buckling of nano-fibre reinforced composites: a re-examination of elastic buckling. J. Mech. Phys. Solids 50, 855-879.
Paulson, S., Falvo, M.R., Snider, N., Helser, A., Hudson, T., Seeger, A., Taylor, R.M., Superfine, R., Washburn, S., 1999. In situ resistance measurements of strained carbon nanotubes. Appl. Phys. Lett. 75, 2936-2938.
Rasekh, M., Khadem, S., Tatari, M., 2010. Nonlinear behaviour of electrostatically actuated carbon nanotube-based devices. J. Phys. D: Appl. Phys. 43, 315301-315311.
Robertson, D.H., Brenner, D.W., Mintmire, J.W., 1992. Energetics of nanoscale graphitic tubules. Phys. Rev. B 45, 12592-12595.
Rochefort, A., Avouris, P., Lesage, F., Salahub, D.R., 1999. Electrical and mechanical properties of distorted carbon nanotubes. Phys. Rev. B 60, 13824-13830.
Ru, C.Q., 2000. Effective bending stiffness of carbon nanotubes. Phys. Rev. B 62, 9973-9976.
Srivastava, D., Menon, M., Cho, K., 1999. Nanoplasticity of single-wall carbon nanotubes under uniaxial compression. Phys. Rev. Lett. 83, 2973-2976.
Tersoff, J., 1986. New empirical model for the structural properties of silicon. Phys. Rev. Lett. 56, 632-635.
Wang, Q., 2004. Effective in-plane stiffness and bending rigidity of armchair and zigzag carbon nanotubes. Int. J. Solids Struct. 41, 5451-5461.
Wang, Q., Varadan, V.K., 2005. Stability analysis of carbon nanotubes via continuum models. Smart Mater. Struct. 14, 281-286.
Wang, X., Wang, X., Xiao, J., 2005. A non-linear analysis of the bending modulus of carbon nanotubes with rippling deformations. Compos. Struct. 69, 315-321.
Wang, Y., Wang, X., Ni, X., 2004. Atomistic simulation of the torsion deformation of carbon nanotubes. Modelling Simul. Mater. Sci. Eng. 12, 1099-1107.
Wang, Y., Wang, X.,Ni, X., Wu, H., 2005. Simulation of the elastic response and the buckling modes of single-walled carbon nanotubes. Computational Mater. Sci. 32, 141-146.
Wang, M.S., Kaplan-Ashiri, I., Wei, X.L., Rosentsveig, R., Wagner, H.D., Tenne, R., Peng, L.M., 2008. In situ tem measurements of the mechanical properties and behavior of WS_2 nanotubes. Nano Res. 1, 22–31.
Xiao, J., Gama, B., Gillespie Jr., J., 2005. An analytical molecular structural mechanics model for the mechanical properties of carbon nanotubes. Int. J. Solids Struct. 42, 3075-3092.
Yakobson, B.I., Brabec, C.J., Bernholc, J., 1996. Nanomechanics of carbon tubes: Instabilities beyond linear response. Phys. Rev. Lett. 76, 2511–2514.
Zaeri, M.M., Ziaei-Rad, S., Vahedi, A., Karimzadeh, F., 2010. Mechanical modelling of carbon nanomaterials from nanotubes to buckypaper. Carbon 48, 3916-3930.
Zhang, H., Wang, L., Wang, J., 2007. Computer simulation of buckling behavior of double-walled carbon nanotubes with abnormal interlayer distances. Computational Mater. Sci. 39, 664-672.

Vitae

Rafael Merli, born 1975, is Civil Engineer and Doctor in Structural Engineering. He is Research Assistant at the Department of Structural Mechanics of the Universidad Politécnica de Valencia (Spain). His research interests cover computational solid mechanics and structural modeling of carbon nanotubes. He is currently investigating nonlinear behavior of carbon nanotubes via atomistic models.

Carlos Lázaro, born 1966, is Civil Engineer and Doctor in Structural Engineering. He is Associate Professor at the Department of Structural Mechanics of the Universidad Politécnica de Valencia (Spain). His research interests cover computational solid mechanics with emphasis on models for slender rods, the design of movable structures and the application of fiber reinforced and recycled concrete to structural design. He is currently investigating nonlinear mechanical modeling of carbon nanotubes. He is Vice-president and Chair of the Technical Activities Committee of the International Association for Shell and Spatial Structures (IASS), and co-founder of the structural design firm CMD Ingenieros.

Salvador Monleón, born 1956, is Civil Engineer and Doctor in Structural Engineering. He is Professor at the Department of Structural Mechanics of the Universidad Politécnica de Valencia (Spain). His research interests cover computational solid mechanics with emphasis on models for slender members, as rods and thin shells, the conceptual design and structural modelling of bridges, and the application of fibre reinforced and recycled concrete to structural design. He is currently investigating nonlinear mechanical modeling of carbon nanotubes and usually collaborates with the structural design firm CMD Ingenieros.

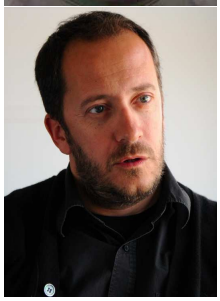

Alberto Domingo, born 1965, is Civil Engineer and Doctor in Structural Engineering. He is a Professor in the Department of Civil Engineering and Design in Construction at the Universidad Politécnica de Valencia (Spain). He has led and developed research projects regarding the behavior of reinforced concrete with steel fibers applied to shell structures, recycled concrete, and analysis of flexible structures with large rotations. He is an active member of the Executive Committee of the International Association for Shell and Spatial Structures (IASS). He is specialist in structural and construction projects, and co-founder of the structural design firm CMD Ingenieros.

Black and white version of color figures

The figure captions including (color on the web) are intended for color reproduction on the web and in black-and-white in print. For this purpose, black and white versions of these figures are supplied next.

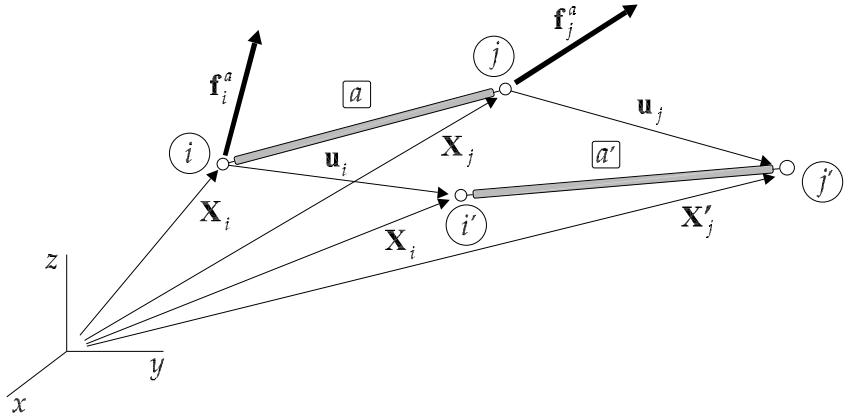

Figure 19: Forces and displacements at the bar ends (color version, fig 2)

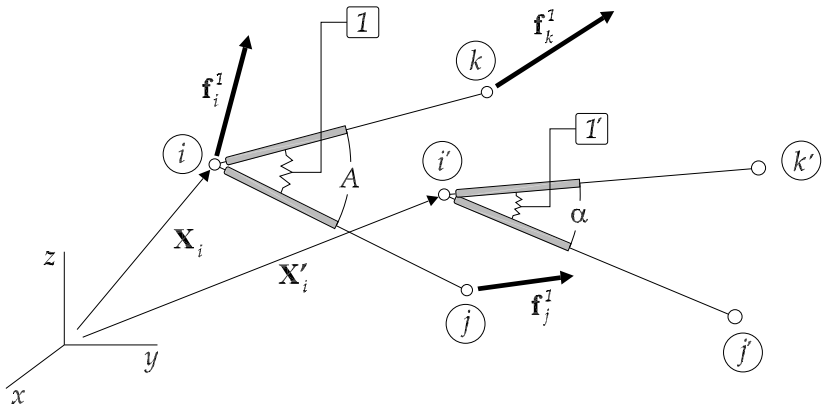

Figure 20: Forces and displacements acting on the spring element (color version, fig 3)

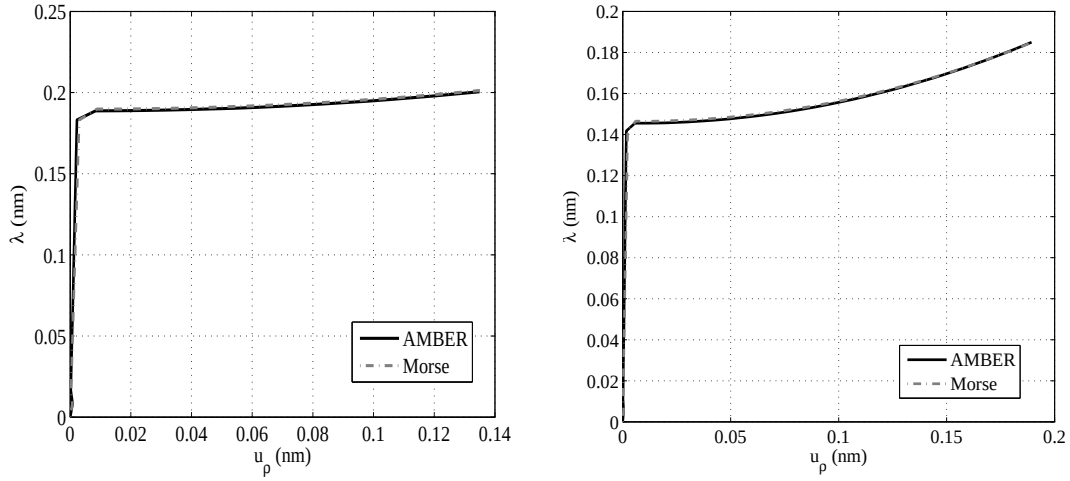

(a) ZigZag(7,0)

(b) Armchair(3,3)

(c) Armchair(4,4)

(d) Chiral(4,2)

Figure 21: Nonlinear equilibrium paths under compression (color version, fig 7)

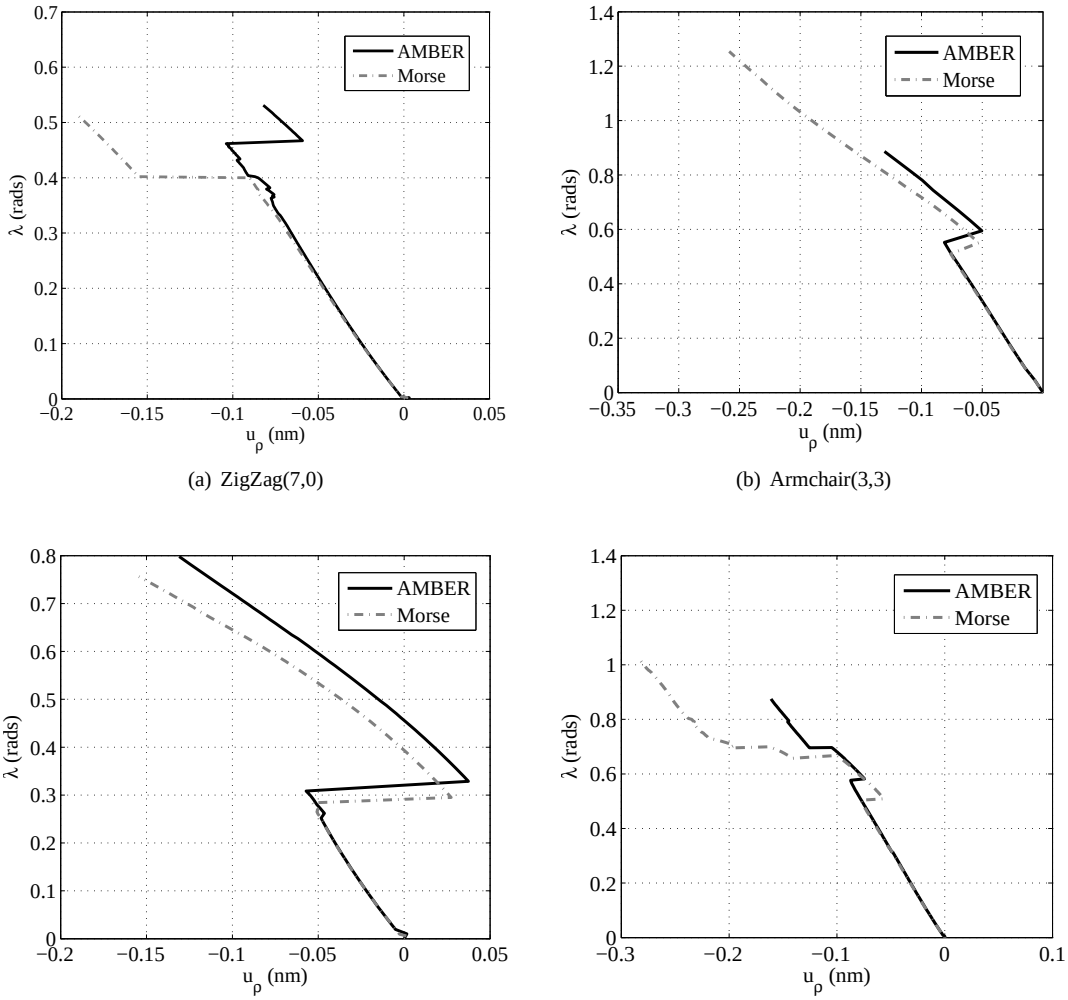

(a) ZigZag(7,0)

(b) Armchair(3,3)

(c) Armchair(4,4)

(d) Chiral(4,2)

Figure 22: Nonlinear equilibrium paths under bending (color version, fig 10)

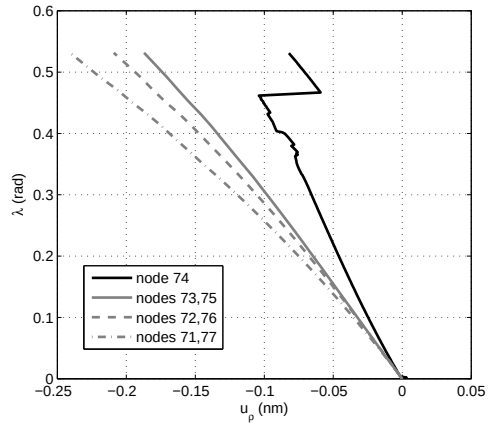

Figure 23: Equilibrium paths (color version, fig 12(b))

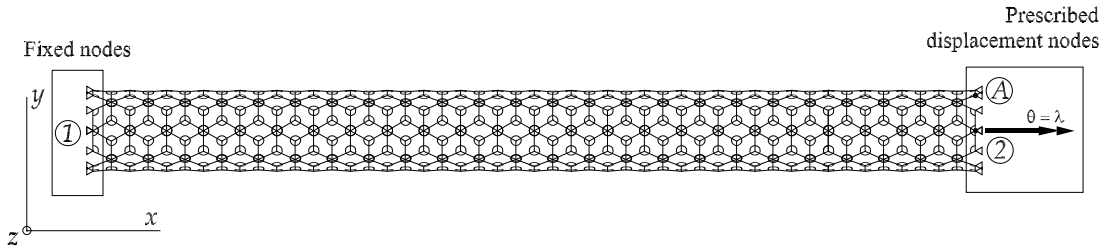

(a) Supporting conditions under torsion

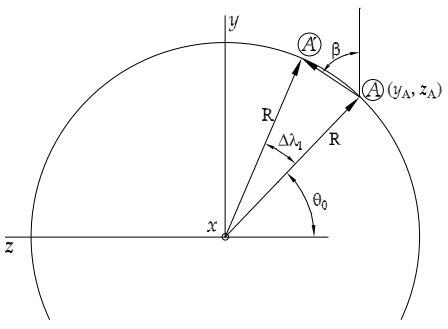

(b) Rotation first increment

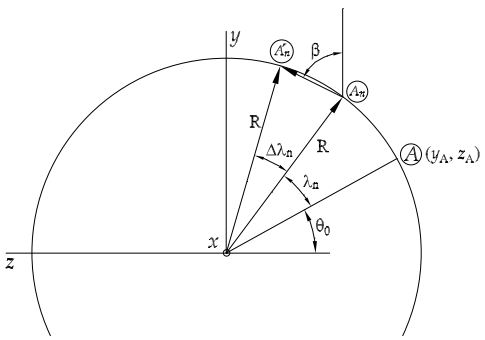

(c) Rotation generic increment

Figure 24: Supporting conditions and imposed displacements schemes (color version, fig 14)

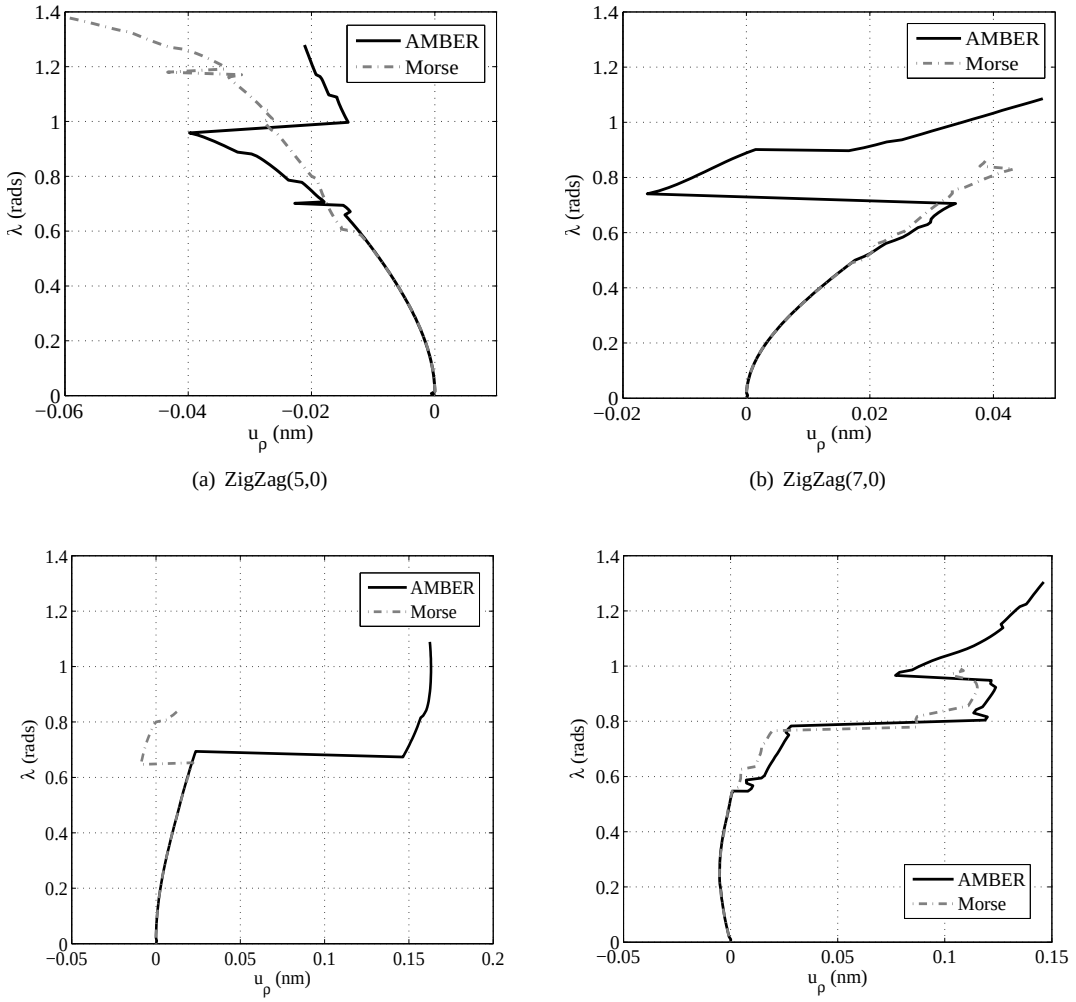

(a) ZigZag(5,0) (b) ZigZag(7,0)

(c) Armchair(4,4) (d) Chiral(5,3)

Figure 25: Nonlinear equilibrium paths under torsion (color version, fig 15)

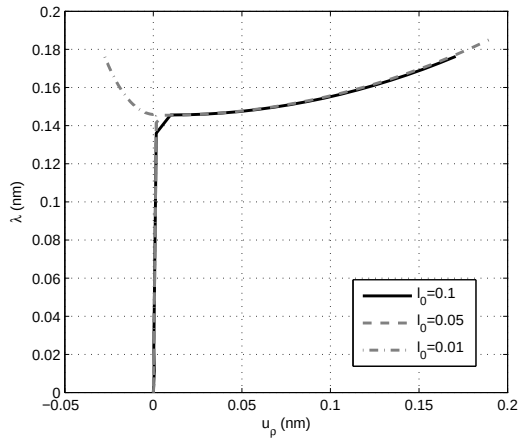

(a) Armchair(3,3) compression

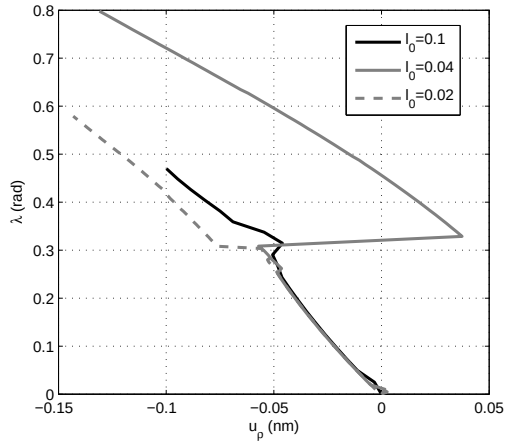

(b) Armchair(4,4) bending

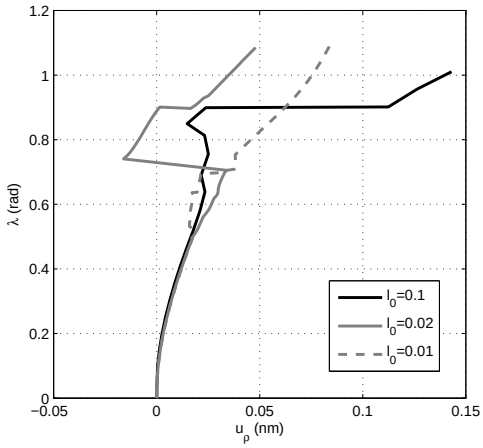

(c) ZigZag(7,0) torsion

Figure 26: Equilibrium paths with different increment size l_0 (color version, fig 17)

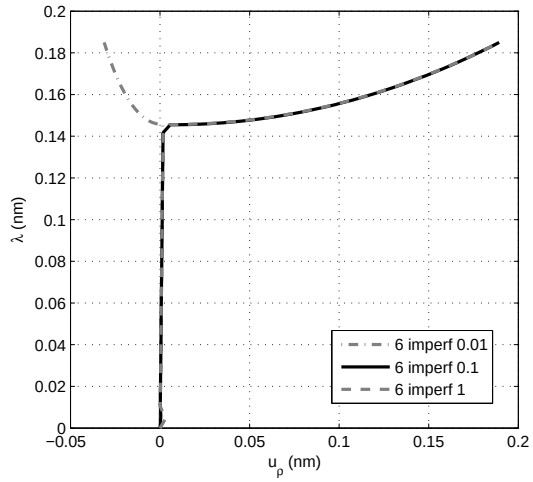

(a) Armchair(3,3) compression

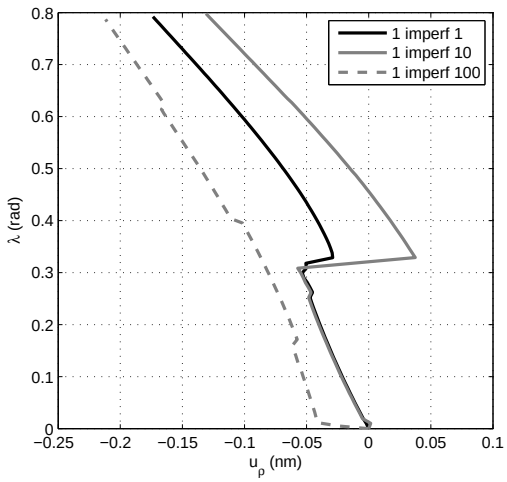

(b) Armchair(4,4) bending

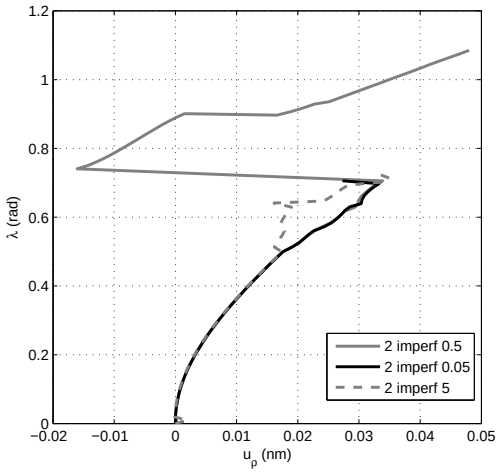

(c) ZigZag(7,0) torsion

Figure 27: Equilibrium paths with different imperfections ϵ (color version, fig 18)